THREE-DIMENSIONAL PRINTING ENGINEERED MATERIALS VIA INTEGRATION OF ULTRASOUND DIRECTED SELF-ASSEMBLY WITH STEREOLITHOGRAPHY

by

John Greenhall

A dissertation submitted to the faculty of
The University of Utah
in partial fulfillment of the requirements for the degree of

Doctor of Philosophy

Department of Mechanical Engineering

The University of Utah

December 2017

The University of Utah Graduate School

STATEMENT OF DISSERTATION APPROVAL

The dissertation of **John Greenhall**

has been approved by the following supervisory committee members:

Bart Raeymaekers	, Chair	**07/25/2017** Date Approved
Fernando Guevara Vasquez	, Member	**07/25/2017** Date Approved
Jake Abbott	, Member	**07/25/2017** Date Approved
Kam Leang	, Member	**07/25/2017** Date Approved
Bruce Gale	, Member	**07/25/2017** Date Approved

and by **Tim Ameel** , Chair/Dean of

the Department/College/School of **Mechanical Engineering**

and by David B. Kieda, Dean of The Graduate School.

ABSTRACT

Engineered materials consisting of nano- or microparticles embedded in a matrix material may exhibit unique physical properties that are attributed to the specific type, geometry, and spatial pattern of the particles. However, existing techniques for fabricating such engineered materials are limited to laboratory scale, specific materials, and/or 2D implementations. We employ ultrasound directed self-assembly (DSA), which relies on the acoustic radiation force associated with an ultrasound wave field of wavelength significantly larger than the particle size, to organize particles of any material type dispersed in a fluid medium, into a user-specified pattern over a macroscale area or volume.

We first derive the dynamics of a single particle in a fluid medium subject to a one-dimensional standing ultrasound wave field. We analyze the trajectory of the particle, driven to either a node or antinode of the ultrasound wave field by the acoustic radiation force, and we show that the particle oscillates around the node of the standing wave with an amplitude that depends on the ratio of the time-dependent drag forces and the particle inertia. We then theoretically derive and experimentally implement a method for single and multidimensional ultrasound DSA, which enables manipulating the position of a single particle and organizing user-specified patterns of nano- and microparticles dispersed in a fluid medium contained within a reservoir lined with ultrasound transducers, respectively. In contrast with existing ultrasound DSA techniques, this method works for any user-specified pattern of particles within a reservoir of arbitrary geometry and ultrasound transducer arrangement. Additionally, the method accounts for all ultrasound wave

reflections in the reservoir, which allows for straightforward experimental implementation of the method.

Finally, we integrate ultrasound DSA with stereolithography to fabricate engineered materials layer-by-layer via stereolithography, where in each layer we organize a user-specified pattern of particles using ultrasound DSA. This process enables manufacturing macroscale 3D materials with a user-specified microstructure consisting of particles of any material. We demonstrate 3D printing macroscale multilayer engineered materials containing a Bouligand microstructure of nickel-coated carbon fibers. Additionally, we fabricate engineered materials containing a pattern of electrically conductive nickel-coated carbon fibers, which illustrates the feasibility of 3D printing structures with embedded insulated electrical wiring. This process has implications for applications including manufacturing of metamaterials, and multifunctional composite materials.

TABLE OF CONTENTS

LIST OF FIGURES

LIST OF TABLES

NOMENCLATURE

In this dissertation, an italic symbol (lowercase or uppercase) denotes a scalar, a bold lowercase symbol denotes a vector or array, and a bold uppercase symbol denotes a matrix.

Symbols

Symbol	Units	Text location	Description
Particle and fluid medium properties			
c_f	m/s	CH 1	Speed of sound in the fluid medium
ρ_f	kg/m^3	CH 1	Density of the fluid medium
β_f	m·s^2/kg	CH 1	Compressibility of the fluid medium
μ_f	kg/(m·s)	CH 2	Dynamic viscosity of fluid medium
c_p	m/s	CH 1-4	Longitudinal speed of sound in the particle
c_τ	m/s	CH 2	Shear speed of sound in the particle
ρ_p	kg/m^3	CH 1	Density of the particle
β_p	m·s^2/kg	CH 1	Compressibility of the particle
r_p	m	CH 1-4	Particle radius
m	kg	CH 2	Particle mass
Φ_ρ	-	CH 1,4	Density contrast factor
Φ_β	-	CH 1,4	Compressibility contrast factor
Φ	-	CH 1-3	Acoustic contrast factor
Reservoir properties and parameters			
Z_t	kg/(m^2·s)	CH 4	Ultrasound transducer acoustic impedance
N_t	-	CH 4	Number of ultrasound transducers
$\tilde{Z}$	-	CH 4	Impedance ratio $\tilde{Z} = \rho_f c_f / Z_t$
L	m	CH 1-5	Reservoir length
D	-	CH 4	Reservoir domain
N_d	-	CH 4	Number of domain points
S	-	CH 4	Reservoir boundary
N_b	-	CH 4	Number of boundary elements
ε	m	CH 4	Length of boundary elements
o	-	CH 4	Reservoir origin
n	-	CH 1,3,4	Surface normal direction
v	m/s	CH 1,3,4	Ultrasound transducer parameter: the complex harmonic velocity of the vibrating ultrasound transducer surface
v	m/s	CH 4	Vector of N_t ultrasound transducer parameters $\mathbf{v} = \left[v_1, v_2, \ldots, v_{N_t} \right]^T$

V	m/s	CH 3	Ultrasound transducer amplitude $V = \|v\|$
ψ	rad	CH 3	Ultrasound transducer phase $\psi = \text{Arg}(v)$
Dimensional and time variables			
x, y, z	m	CH 1-5	Coordinates with respect to the reservoir origin **o**
$\mathbf{x}$	m	CH 4	3D point $\mathbf{x} = [x, y, z]^T$ within the reservoir domain D or on the boundary S
$\mathbf{q}$	m	CH 4	3D point $\mathbf{q} = [x, y, z]^T$ on the boundary S
r, θ	m, rad	CH 2,3	Polar coordinates
X	m	CH 2	x-direction coordinate with respect to the nearest node of the ultrasound wave field
x_s, $\mathbf{x}_s$	m	CH 1-4	Particle position at steady-state
t	s	CH 2	Time
Ultrasound parameters and variables			
ω	rad/s	CH 1-4	Ultrasound wave field frequency
λ	m	CH 1-5	Ultrasound wave field wavelength in the fluid medium $\lambda = 2\pi c_f / \omega$
k	m^{-1}	CH 1-4	Wave number in the fluid medium $k = \omega / c_f$
T	s	CH 1,2,4	Period of the ultrasound wave field $T = 2\pi / \omega$
φ	m^2/s	CH 1-4	Velocity potential of an incident ultrasound wave field
φ_{sc}	m^2/s	CH 1-2	Velocity potential of a scattered ultrasound wave field
φ_{tot}	m^2/s	CH 1-2	Total velocity potential field, $\varphi_{tot} = \varphi + \varphi_{sc}$
$\boldsymbol{\varphi}$	m^2/s	CH 3	Vector of incident velocity potential φ values at N_d domain points in the domain D
P, **A**, **B**	m	CH 4	The boundary element matrices used to calculate $\boldsymbol{\varphi}$ in the domain D as a function of **v** along the boundary S
φ_0	m^2/s	CH 1-3	Velocity potential amplitude
p	$kg/(m \cdot s^2)$	CH 1	Fluid pressure
p_0	$kg/(m \cdot s^2)$	CH 1	Pressure amplitude
$\mathbf{u}$	m/s	CH 1,2	Fluid velocity vector
u_0	m/s	CH 1	Velocity amplitude
$\overline{u}$	m/s	CH 2	1D fluid velocity averaged across the surface of a spherical particle
δp	$kg/(m \cdot s^2)$	CH 1	Radiation pressure
$G(\mathbf{x},\mathbf{q})$	m^2/s	CH 4	Green's function representing the free-field ultrasound wave from a point acoustic source at **x**, measured at point **q**
Particle dynamics terms			
$\mathbf{f}$	N	CH 1,4	3D acoustic radiation force
F_r	N	CH 2	1D acoustic radiation force
C_r	N	CH 2	Acoustic radiation force coefficient
X_{des}	-	CH 3	The set of desired points defining a user-specified pattern of particles
U	N·m	CH 3	Radiation potential
$\overline{U}$	N·m	CH 3	Average radiation potential for all points in the desired set X_{des}
$\mathbf{Q}$	$N \cdot s^2/m$	CH 3	Hermitian matrix used to compute U as a function of **v**
$\overline{\mathbf{Q}}$	$N \cdot s^2/m$	CH 3	Average Hermitian matrix used to compute $\overline{U}$ as a function of **v**
F_d	N	CH 2	Drag force
C_s	kg/s	CH 2	Stokes drag coefficient
C_o	kg/m	CH 2	Oseen drag coefficient

ζ	-	CH 2	Damping coefficient of a second order dynamical system
ω_n	rad/s	CH 2	Natural frequency of a second order dynamical system
T_s	s	CH 2	Settling time of a second order response
M_p	%	CH 2	Percent overshoot of a second order response
$\tilde{x}$	m	CH 2	Amplitude of steady-state oscillations
K_1	-	CH 2	Ratio between the acoustic radiation force and time-independent Stokes drag force
K_2	-	CH 2	Ratio between the time-dependent Stokes and Oseen damping forces and the particle inertia
Miscellaneous parameters, variables, and mathematical functions			
θ_d	rad	CH 5	Desired alignment direction
h_0	m	CH 5	Initial cured resin layer thicknesses
h_f	m	CH 5	Final cured resin layer thicknesses
V_{app}	V	CH 5	Applied electrical voltage
I_m	A	CH 5	Measured electrical current
i	-	CH 1-4	Imaginary unit $i = \sqrt{-1}$
$H_0(\cdot)$	-	CH 4	0^{th} order cylindrical Hankel function of the first kind
A_n, B_n, G_n	A.U.	CH 2	Spherical harmonic coefficients of order n
$j_n(\cdot)$	-	CH 2	n^{th} order spherical Bessel function
$h_n(\cdot)$	-	CH 2	n^{th} order spherical Hankel function of the first kind
$P_n(\cdot)$	-	CH 2	n^{th} order Legendre polynomial
$\Gamma(\cdot)$	-	CH 2	Gamma function
$\langle\cdot\rangle$	-	CH 1-4	Time average over one period T of the ultrasound wave field

Acronyms

Acronym	Text location	Description
1D	CH 1-3	One-dimensional
2D	CH 1,4,5	Two-dimensional
3D	CH 5	Three-dimensional
DNA	CH 1	Deoxyribonucleic acid
DSA	CH 1-5	Directed self-assembly
CT	CH 5	Computed tomography
FFT	CH 5	Fast Fourier transformation
SEM	CH 1	Scanning electron microscopy
SLA	CH 1,5	Stereolithography
UV	CH 5	Ultraviolet

ACKNOWLEDGEMENTS

I would like acknowledge Bart Raeymaekers and Fernando Guevara Vasquez for their advice and mentorship, which was vital to my growth as an engineer, researcher, and writer. Additionally, I acknowledge the financial support provided to me by Army Research Office Contract# No. W911NF-14-1-0565 and the NASA Space Technology Research Fellowship Award# No. NNX15AP30H. Last but not least, I would like to acknowledge my mother, uncles, and friends for keeping me positive and focused throughout my graduate career.

CHAPTER 1

INTRODUCTION

1.1. Motivation

Engineered materials consisting of specifically designed patterns of nano- or microparticles embedded in a matrix material are of great interest to the science and engineering community due to their unique mechanical [1.1], electrical [1.2], thermal [1.3], acoustic [1.4], and/or electromagnetic properties [1.5]. These unique properties arise from the interaction of the particles with themselves, with the matrix, and with an external field. The material type, shape, and geometric configuration of the nano- or microparticles embedded in the engineered material then enable tailoring the properties of the material. Figure 1.1 shows examples of engineered materials with unique physical properties, including a negative optical refraction index achieved by creating a periodic pattern of voids in a pair of parallel metallic plates (Fig. 1.1(a)) [1.6], a negative acoustic refraction index implemented by a dual layer material with spiral-shaped inclusions (Fig. 1.1(b)) [1.7], and high tensile mechanical strength obtained by aligning carbon nanotubes within a polymer matrix (Fig. 1.1(c)) [1.8].

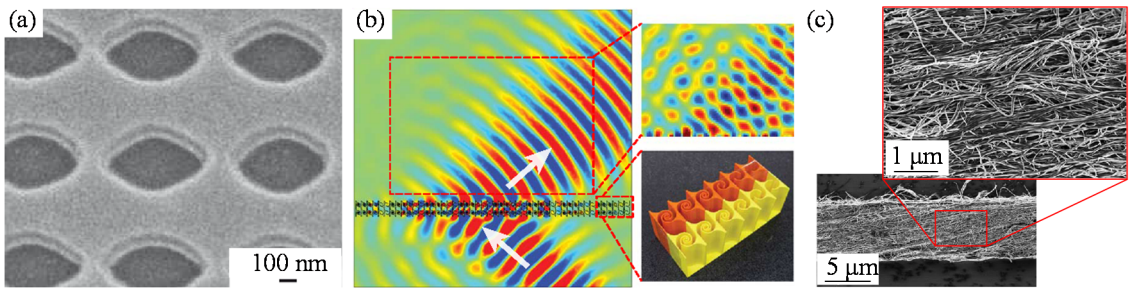

Figure 1.1: Engineered materials with unique physical properties. (a) Scanning electron microscope (SEM) image of a negative-index optical metamaterial consisting of a pair of metallic plates with periodic voids [1.6]. (b) Simulated pressure (color) of an ultrasound wave field incident to a negative-index acoustic metamaterial with inset images showing a close-up of the simulated ultrasound wave field (top), and a photograph of the metamaterial (bottom) [1.7]. (c) SEM image of a composite material consisting of aligned carbon nanotubes embedded in a polymer matrix, resulting in ultrahigh tensile strength [1.8]. Images adapted with permission from the references as indicated: (a) Copyright 2006 the Optical Society; (b) Copyright 2014 Nature Publishing Group; (c) Copyright 2012 the Royal Society of Chemistry.

Engineered materials with unique physical properties find application in acoustic and electromagnetic cloaking [1.4], [1.9] and subwavelength imaging [1.10], [1.11], and multifunctional composite materials with tailored mechanical and electrical properties [1.8], among other applications. However, implementation of such materials is restricted to theoretical and laboratory-scale demonstrations as existing manufacturing techniques used to fabricate engineered materials limit the scalability and/or the range of achievable patterns of nano- or microparticles.

1.2. Research objective

The critical science problem that inhibits mass processing and manufacturing of engineered materials with unique physical properties is organizing large quantities of nano- or microparticles into user-specified patterns within a matrix material. Several methods have been documented in the literature that attempt to address this problem, including methods based on electric, flow, and magnetic fields. However, these methods do not enable organizing user-specified patterns of particles over a macroscale volume or area, which precludes fabricating engineered materials for macroscale engineering applications.

In contrast, in this dissertation we demonstrate a directed self-assembly (DSA) method based on a standing ultrasound wave field to achieve quasi-instantaneous organization of large quantities of nano- or microparticles into a macroscale pattern in a liquid resin medium, which is subsequently cured via stereolithography (SLA) to 3D print a macroscale engineered material with complex 3D geometry and tailored microstructure.

Thus, the objective of this dissertation is threefold:

(1) Derive a theoretical model to describe the motion of a single nano- or microparticle in a fluid medium, driven by the acoustic radiation force associated with an

ultrasound wave field, and characterize the transient and steady-state behavior of the particle/fluid system.

(2) Derive an ultrasound DSA method to manipulate a single nano- or microparticle in a fluid medium, and to organize large quantities of nano- or microparticles into user-specified patterns in a fluid medium, and experimentally validate the method.

(3) Integrate ultrasound DSA with stereolithography additive manufacturing to 3D print macroscale polymer matrix engineered materials of complex 3D geometry and with a user-specified microstructure.

1.3. Significance

Accomplishing the research objective will enable 3D printing of macroscale engineered materials consisting of a polymer matrix with a microstructure based on a user-specified pattern of particles. The ability to manufacture macroscale engineered materials with a specific microstructure will have a significant impact in a broad range of engineering applications, including fabricating materials for acoustic and electromagnetic cloaking and subwavelength imaging, as well as rapid-manufacturing of devices and materials with high mechanical strength and/or embedded electrical wiring, to only name a few. In particular, the ability to 3D print devices with high mechanical strength and/or embedded electrical wiring has applications in hard-to-reach areas, such as extraterrestrial sites, where fabricating and transporting small quantities of parts through traditional means is costly and time consuming, and in-situ manufacturing is the preferred approach.

Additionally, a theoretical understanding of the ultrasound DSA process will lead to improved and new processing and sorting technologies in biology, biomedical engineering, and process control, where large quantities of nano- or microparticles must be manipulated

and organized quasi-instantaneously without physical contact (see Sec.1.5).

1.4 Background

1.4.1 Directed self-assembly

Directed self-assembly (DSA) is defined as the process by which nano- or microparticles or other discrete components spontaneously organize due to interactions between the components and their environment, driven by internal or external forces [1.12]. DSA is typically categorized into templated, template-free, or external field-directed techniques [1.13].

Figure 1.2(a) shows the templated DSA process, which is based on mechanical [1.14] or chemical [1.15] modification of the surface of a substrate to create regions of attraction that selectively prompt particle deposition on that substrate. Additionally, we distinguish between a soft template, where user-specified regions of attraction on the substrate surface determine the pattern of particles that is assembled, and a hard template, where the geometry of the substrate surface controls the pattern of particles that is assembled [1.16]. Figure 1.2(b) shows an example of a soft template that consists of a silicon oxide substrate

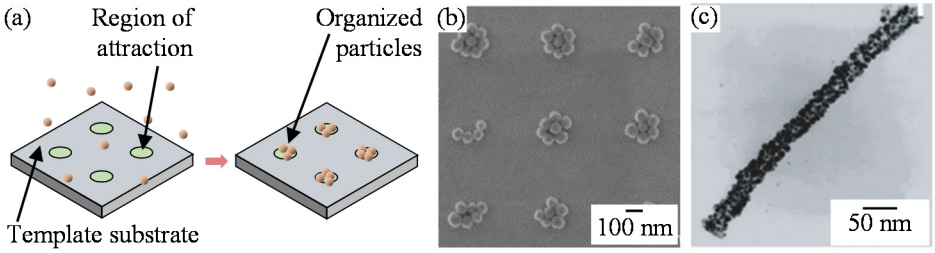

Figure 1.2: Templated directed self-assembly. (a) Process for organizing patterns of particles. (b) Soft template consisting of a silicon oxide substrate with chemically functionalized regions of attraction to prompt deposition of silica nanoparticles in a dot pattern [1.17]. (c) Hard template consisting of a tobacco mosaic virus substrate, which attracts gold nanoparticles to deposit in a cylindrical pattern on the virus surface [1.18]. Images adapted with permission from the references as indicated: (b) Copyright 2010 John Wiley and Sons; (c) Copyright 2003 American Chemical Society.

with periodically spaced regions of attraction that prompt silica nanoparticles to deposit on the substrate surface in a dot pattern [1.17]. Figure 1.2(c) shows an example of a hard template that consists of a tobacco mosaic virus with regions of attraction spread uniformly over the virus surface to prompt deposition of gold nanoparticles in a cylindrical pattern [1.18]. Because of the intricacy of the manufacturing techniques used to create templates, most templated DSA methods limit template sizes to nano- or micrometers. Block-copolymer templates have been used to assemble macroscale patterns of nanoparticles, but this often requires complex chemical modification to ensure compatibility between the block-copolymers and the particles, which limits the practical feasibility of the method [1.19], [1.20].

Figure 1.3(a) illustrates the template-free DSA process, which relies on capping molecules that selectively interact with each other and with the particles to create organized nano- or microstructures [1.13]. Figure 1.3(b) shows an example of template-free DSA, where deoxyribonucleic acid (DNA) capping molecules are utilized to align gold nanorods [1.22]. The interactions between the capping molecules and the particles are controlled through external stimuli such as light [1.23], temperature [1.21], and acidity-level [1.24], which allows user-controlled assembling or disbanding of the nano- or

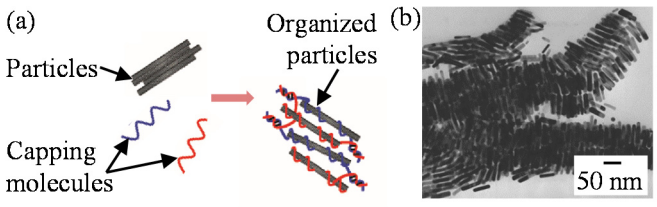

Figure 1.3: Template-free directed self-assembly. (a) Process for organizing patterns of particles [1.21] such as (b) scanning electron microscope image of gold nanorods aligned using deoxyribonucleic acid (DNA) capping molecules [1.22]. Images adapted with permission from the references as indicated: (a) Copyright 2007 American Chemical Society; (b) Copyright 2001 The Royal Chemical Society.

microstructures. However, since selection of the material properties and geometry of the capping molecule and particle pair determine the final organized pattern of particles, it is not practically feasible to tailor the resulting nano- or microstructure that is assembled.

Figure 1.4 shows examples of patterns of particles organized via external field DSA techniques, which utilize external interactions such as convective forces [1.25], electric fields [1.26], magnetic fields [1.27], or standing ultrasound wave fields to organize patterns of particles [1.28]–[1.31]. Convective forces in a thin liquid film prompt particles to deposit on a substrate in highly concentrated patterns that are controlled by the geometry of the particles and/or the substrate. Figure 1.4(a) shows a scanning electron microscope (SEM) image (left) and a schematic of a side-view (right) of polystyrene nanospheres organized into a close-packed hexagonal configuration along parallel channels machined on the surface of a polydimethylsiloxane substrate using convective forces [1.25]. However, the pattern of particles that is organized is dependent on the geometry of the particles and the surface of the substrate, which inhibits controlling the patterns of particles that are assembled [1.25]. Electric and magnetic fields have been used to create nanostructures such as gold nanowires (Fig. 1.4(b)) [1.26] and chains of magnetic Janus particles (Fig.

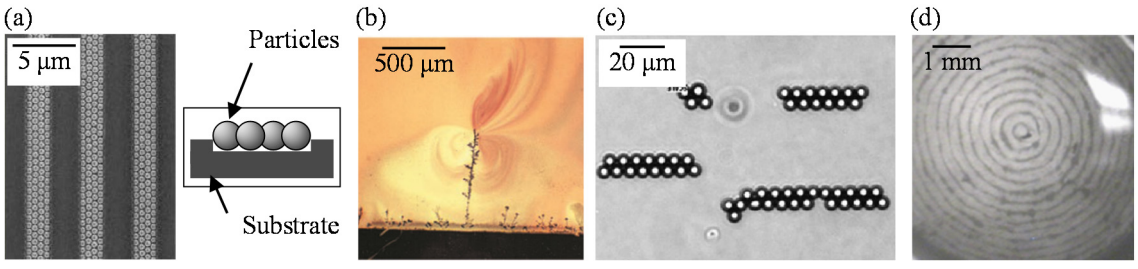

Figure 1.4: External field directed self-assembly. Patterns of particles organized via external field directed self-assembly techniques that employ (a) convective forces [1.25], and (b) electric [1.26], (c) magnetic [1.27], and (d) ultrasound fields [1.28]. Images adapted with permission from the references as indicated: (a) Copyright 2007 American Chemical Society; (b) Copyright 2001 AAAS; (c) Copyright 2009 The Royal Chemical Society; (d) Copyright 2011 AIP Publishing LLC.

1.4(c)) [1.27], but these methods are limited to assembling patterns of nanoparticles with favorable electric and magnetic properties. Additionally, they require ultrahigh amplitude electric or magnetic fields, which limits the scalability of the techniques to cover macroscale areas or volumes. Alternatively, ultrasound DSA employs standing ultrasound wave fields to assemble particles dispersed in a fluid medium into user-specified patterns, such as concentric circular patterns of diamond nanoparticles (Fig. 1.4(d)) [1.28]. Only low-amplitude ultrasound waves are needed, thus enabling scalability to cover macroscale areas and volumes. In addition, ultrasound DSA works independent of the physical properties of the particles [1.28]–[1.31].

1.4.2 Ultrasound directed self-assembly

Ultrasound DSA organizes particles dispersed in a fluid medium into patterns by means of the acoustic radiation force generated when a standing ultrasound wave field scatters off the particles [1.30]. To understand the ultrasound DSA process, we require a theoretical model that relates the ultrasound wave field to the resulting patterns of particles. This section explains how ultrasound DSA can be employed to organize patterns of nano- or microparticles by first introducing the ultrasound wave field (Sec. 1.4.2.1), ultrasound scattering (Sec. 1.4.2.2), and then describing the acoustic radiation force and how it drives particles into a pattern (Sec. 1.4.2.3).

1.4.2.1 *Ultrasound wave field*

An ultrasound wave field is defined as an acoustic (pressure) wave field with a frequency that exceeds 20 kHz, which is the maximum sound frequency that can be registered by humans [1.32]. Such a wave field comprises mechanical vibrations that propagate through a compressible solid or fluid medium and results in local regions of

compression and rarefaction. Figure 1.5(a) shows the regions of compressed and rarefied fluid molecules (not drawn to scale), which are spaced periodically every wavelength λ of the ultrasound wave field. Figure 1.5(b) shows the pressure p corresponding to the ultrasound wave field in Fig. 1.5(a), where p_0 is the pressure amplitude of the ultrasound wave field. Figures 1.5(c) and (d) illustrate the difference between traveling ultrasound waves (Fig. 1.5(c)), which propagate through the fluid medium as a function of time t, and standing ultrasound waves (Fig. 1.5(d)), which oscillate in place, and do not propagate through the fluid medium.

Figure 1.6 shows a 2D reservoir of arbitrary geometry lined with ultrasound transducers and filled with a fluid medium, which represents a setup used for ultrasound DSA. We apply a sinusoidal voltage to each ultrasound transducer, which causes the ultrasound transducer surface to vibrate like a piston source and generate ultrasound waves in the fluid medium. The traveling ultrasound waves propagate through the reservoir and reflect off the reservoir walls, which results in a standing ultrasound wave field in the fluid medium.

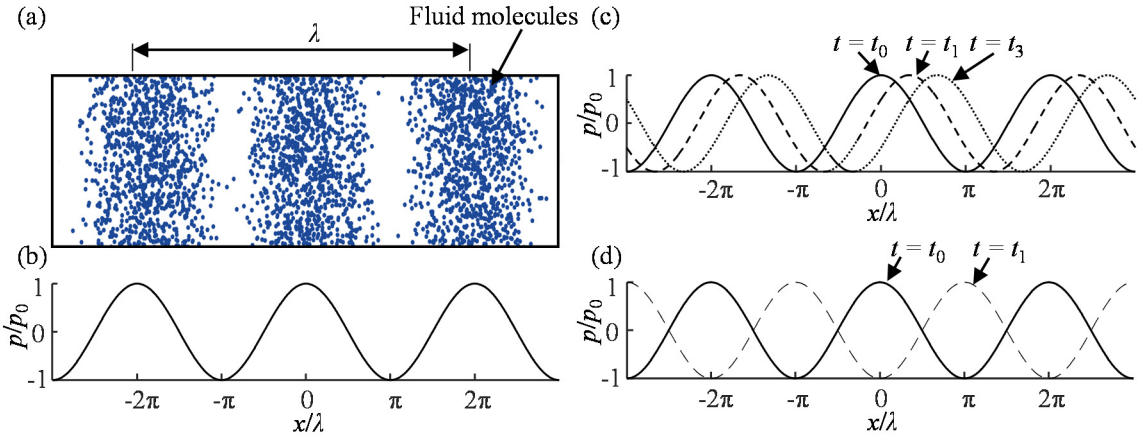

Figure 1.5: Ultrasound waves in a fluid medium. (a) Regions of compressed and rarefied fluid molecules (not drawn to scale) are spaced every wavelength λ, which results in (b) a sinusoidal pressure p wave in the fluid medium, where p_0 is the wave amplitude. (c) A traveling ultrasound wave that propagates through the fluid medium as a function of time t. (d) A standing ultrasound wave field that oscillates in place as a function of t.

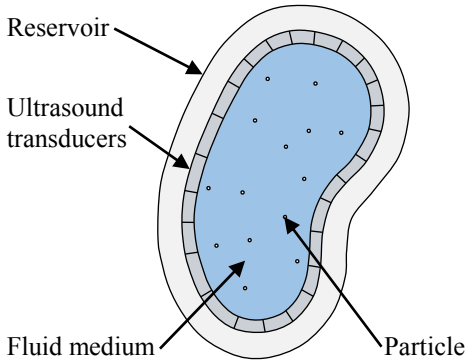

Figure 1.6: Schematic of a 2D reservoir used in ultrasound directed self-assembly applications.

We calculate the ultrasound wave field φ within the fluid medium of density ρ_f and sound speed c_f by solving the Helmholtz equation [1.33]

$$\varphi + k^2 \nabla^2 \varphi = 0. \tag{1.1}$$

Here φ is the velocity potential in the fluid medium and $k = \omega/c_f$ is the wave number of the ultrasound wave field with frequency ω. In Eq. (1.1), the Helmholtz equation is derived assuming that the ultrasound wave field consists of small amplitude, adiabatic vibrations, and that the pressure and density of the fluid medium are proportional [1.32]. These assumptions are not strictly valid, but they closely approximate the conditions in common ultrasound DSA applications [1.28]–[1.32], [1.34]. At the interface between the fluid medium and ultrasound transducers the ultrasound wave in the fluid medium is constrained by the impedance boundary condition [1.32]

$$\mathbf{n} \bullet \nabla \varphi + ik\tilde{Z}\varphi = v\,, \tag{1.2}$$

where $\tilde{Z} = \rho_f c_f / Z_t$ is the impedance mismatch between the fluid medium and the ultrasound transducer with acoustic impedance Z_t. Additionally, v is the complex harmonic

velocity of the ultrasound transducer as it vibrates in the direction **n** normal to the ultrasound transducer surface.

To calculate the ultrasound wave field within a reservoir lined with ultrasound transducers we simultaneously solve the Helmholtz equation (Eq. (1.1)) within the reservoir and the impedance boundary condition (Eq. (1.2)) at the interface between the fluid medium and ultrasound transducer surface. In a reservoir with 1D geometry and two ultrasound transducers that oppose each other, the ultrasound wave field can be calculated analytically (see Ch. 2-3) [1.33]. Alternatively, in most engineering applications with 2D or 3D reservoir geometries and large (> 2) numbers of ultrasound transducers (see Ch. 4-5), the ultrasound wave field within a reservoir is typically computed using numerical techniques such as the boundary element method (see Ch. 4) [1.35] or the finite element method [1.36].

1.4.2.2 *Scattering of ultrasound wave fields*

Figure 1.7 shows a particle submerged in a fluid medium and subjected to an incident wave field φ that reflects and refracts at the surface of the particle, which generates a reflected ultrasound wave field φ_r in the fluid medium and a transmitted ultrasound wave field φ_{tr} in the particle. The transmitted ultrasound wave field then propagates through the particle to an opposing surface of the particle, where it reflects back into the particle (φ'_{tr}) and refracts into the fluid medium (φ''_{tr}). The refracted wave continues to propagate through the particle, where it reflects and refracts each time it encounters the particle surface. This results in a scattered ultrasound wave field φ_{sc} that consists of the initial reflected ultrasound wave field φ_r and all of the ultrasound wave fields that propagate through the particle and refract back into the fluid medium (φ''_{tr}).

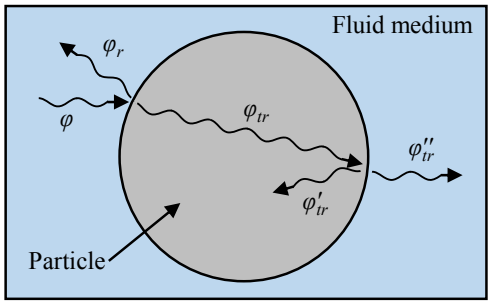

Figure 1.7: Ultrasound reflection and refraction off a particle submerged in a fluid medium. A particle submerged in a fluid medium and subject to an incident ultrasound wave field φ that reflects and refracts at the particle surface and generates a reflected ultrasound wave field φ_r and a transmitted ultrasound wave field φ_{tr}, which propagates through the particle

Scattering of waves has been analyzed for a compressible elastic spherical particle of radius r_p subject to a plane ultrasound wave field of wavelength λ in an inviscid fluid medium [1.37]–[1.39]. In this analysis, the incident φ and scattered ultrasound wave field φ_{sc} are represented as an infinite-series spherical harmonic expansion (see Ch. 2 for details) [1.39], [1.40]. The scattered ultrasound wave field is computed by satisfying the boundary conditions at the interface between the spherical particle and the fluid medium, where the following conditions hold [1.39]:

(1) There is no fluid penetration in the spherical particle.

(2) The shear stress at the surface of the spherical particle is zero.

(3) The pressure in the fluid medium is equal to the normal stress in the spherical particle.

Three distinct regimes of ultrasound scattering exist, differentiated by the ratio of the spherical particle radius r_p and the wavelength λ of the incident ultrasound wave:

(1) Ray regime scattering occurs when the particle radius is significantly larger than the wavelength of the ultrasound wave ($r_p \gg \lambda$).

(2) Mie regime scattering occurs when the particle radius is of the same order as the

wavelength of the ultrasound wave ($r_p \approx \lambda$).

(3) Rayleigh regime scattering occurs when the particle radius is significantly smaller than the wavelength of the ultrasound wave ($r_p \ll \lambda$) [1.38].

In this dissertation, we attempt to organize patterns of nano- and microparticles in a scalable manner. Thus, we utilize low-frequency ultrasound wave fields ($\omega/2\pi < 2.0$ MHz) to mitigate acoustic attenuation, which is proportional to ω^2 [1.32], and to preclude cavitation, which disrupts the patterns of particles formed with ultrasound DSA [1.41]. Hence, this dissertation focuses on ultrasound scattering in the Rayleigh regime.

Figure 1.8 shows a plane ultrasound wave field φ of wavelength λ propagating in the x-direction, incident to a spherical particle of radius $r_p = \lambda/1000$ (Fig. 1.5(a)), which results in a scattered ultrasound wave field φ_{sc} (Fig. 1.8(b)) in the Rayleigh regime. The scattered ultrasound wave field in Fig. 1.8(b) is shown as polar plot around the spherical particle at the origin ($x = 0$) as a function of the spherical particle angle, where the direction of the incident plane ultrasound wave field is indicated by a red arrow. In the Rayleigh regime ($r_p \ll \lambda$), the change in amplitude and phase of the incident ultrasound wave field across the surface of the spherical particle is approximately linear (Fig. 1.8(a)). This results in a scattered ultrasound wave field with quasi-symmetric amplitude in front of and behind the spherical particle (Fig. 1.8(b)). Thus, the spherical harmonic expansion model of the ultrasound wave field can be accurately approximated as a monopole-dipole source, which greatly simplifies computation of the scattered ultrasound wave field [1.42].

1.4.2.3 *Acoustic radiation force*

The force acting on spherical particle in an ultrasound wave field has been studied extensively in the literature [1.42]–[1.48]. When an ultrasound wave field scatters off a

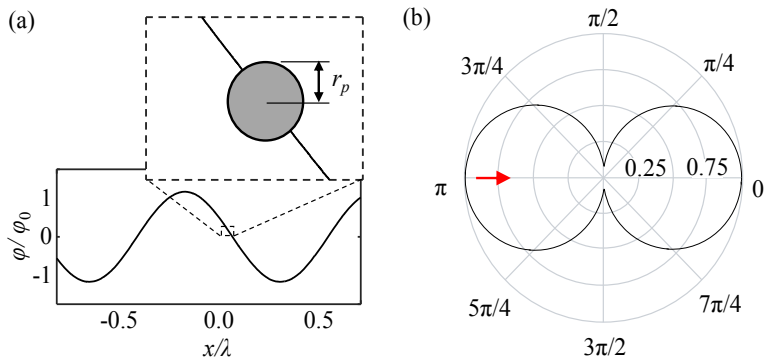

Figure 1.8: Rayleigh regime ultrasound scattering off a spherical particle. (a) Incident ultrasound wave field φ and (b) scattered ultrasound wave field amplitude $|\varphi_{sc}|$ resulting from Rayleigh regime ultrasound scattering ($r_p = \lambda/1000$) for a spherical particle of radius r_p and ultrasound wave field of wavelength λ. (a) The incident ultrasound wave field φ is shown as a function of the normalized distance x/λ from the origin of the spherical particle (gray). (b) A polar plot of the normalized amplitude of the scattered ultrasound wave field φ_{sc} is shown as a function of the spherical particle angle, with the direction of the incident plane ultrasound wave field indicated by a red arrow.

spherical particle, momentum is transferred from the ultrasound wave field to the spherical particle via radiation pressure applied to the surface of the spherical particle [1.43]. Figure 1.9 shows a spherical particle in an incident ultrasound wave field φ (color) (not drawn to scale), which scatters off of the particle surface resulting in a time-averaged radiation pressure $\delta p = \frac{1}{2}\left\langle \rho_f \left|\mathbf{u}_{tot}\right|^2 - \beta_f \left|p_{tot}\right|^2 \right\rangle$ across the spherical particle surface (polar plot). Here, p_{tot} and $\mathbf{u}_{tot}$ are the pressure and velocity, respectively, of the total ultrasound wave (incident plus scattered), and the angled brackets indicate a time-average over one period $T = 2\pi/\omega$ of the ultrasound wave field. The inset image in Fig. 1.9 shows that the radiation pressure δp applied over a differential element dS_p of the spherical particle surface results in a force (black arrows) normal to the spherical particle surface. By summing the forces acting across the surface of the spherical particle, we calculate the net acoustic radiation force **f** acting on the spherical particle (red arrow).

In the Rayleigh regime, the acoustic radiation force acting on an elastic spherical

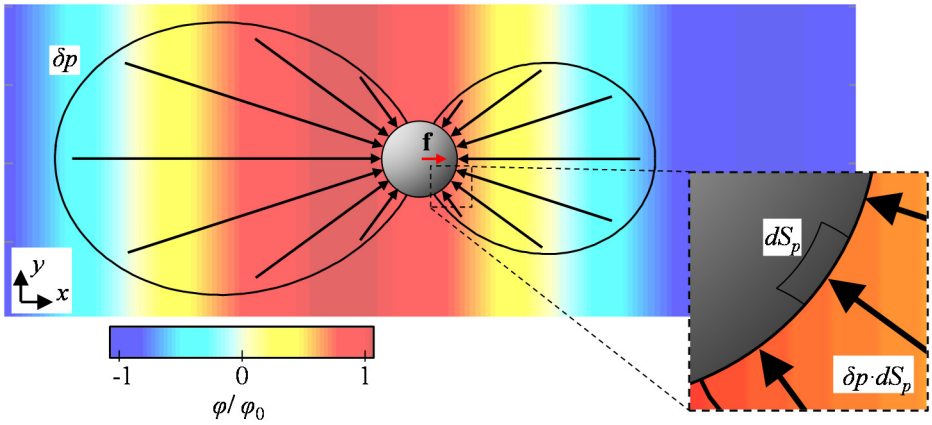

Figure 1.9: Acoustic radiation force acting on a spherical particle in an ultrasound wave field. A spherical particle (gray) in an incident plane standing ultrasound wave field φ (color), which scatters off of the spherical particle surface S_p and results in radiation pressure δp across the surface. The radiation pressure applied over differential surface elements dS_p results in forces normal to the spherical particle surface. The sum of these surface forces is the acoustic radiation force **f** acting on the spherical particle.

particle is calculated using a method first proposed by Gor'kov [1.42]. The method uses a monopole-dipole model to approximate the scattered ultrasound wave field (see Sec. 1.4.2.2), which results in a formulation of the acoustic radiation force as a function of the incident ultrasound wave field φ only. Using Gor'kov's method, the acoustic radiation force **f** is calculated as [1.42], [1.46]

$$\mathbf{f} = -\nabla U, \tag{1.3}$$

where U is the radiation potential of the incident ultrasound wave field shown as

$$U = 2\pi r_p^3 \left(\frac{1}{3} \beta_f \Phi_\beta \left\langle |p|^2 \right\rangle - \rho_f \Phi_\rho \left\langle |\mathbf{u}|^2 \right\rangle \right). \tag{1.4}$$

Here, the subscripts p and f refer to the particle and fluid medium, respectively, $\beta = 1/(\rho c^2)$ is the compressibility of the material with density ρ and sound speed c. Additionally, $\langle |p|^2 \rangle$ and $\langle |\mathbf{u}|^2 \rangle$ are the mean-square fluctuations of the pressure and fluid velocity amplitudes of

the incident ultrasound wave field φ over one period T of the standing wave. The compressibility and density contrast factors are given as

$$\Phi_\beta = 1 - \frac{\beta_p}{\beta_f}, \text{ and} \tag{1.5}$$

$$\Phi_\rho = \frac{\rho_p - \rho_f}{2\rho_p + \rho_f}, \tag{1.6}$$

respectively. The acoustic radiation force drives the particles to the steady-state positions $\mathbf{x}_s$ where $|\mathbf{f}| = 0$ and points toward $\mathbf{x}_s$ in the surrounding region. The acoustic contrast factor is given as

$$\Phi = \Phi_\beta + 3\Phi_\rho, \tag{1.7}$$

and determines whether the particles are driven to the nodes ($\Phi > 0$) or antinodes ($\Phi < 0$) of the standing ultrasound wave field. The steady-state position of the particles corresponds to locations where the radiation potential U is locally minimum. Figure 1.10 shows

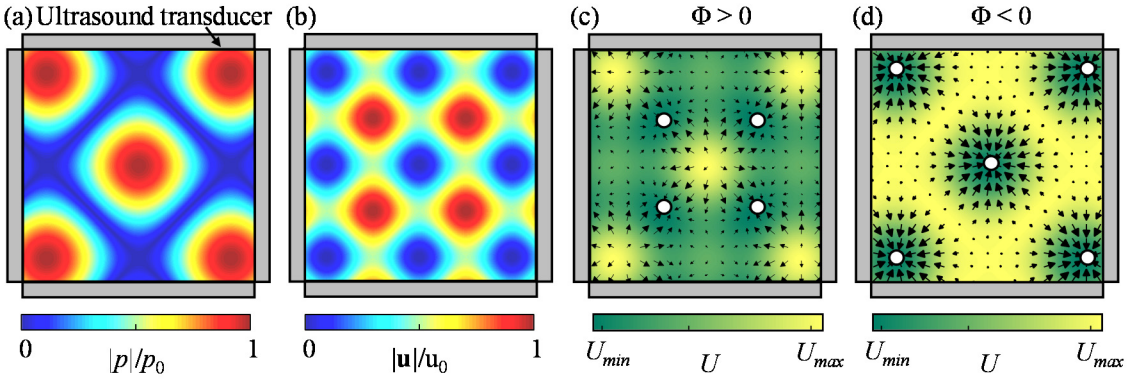

Figure 1.10: Patterns of particles organized by a two-dimensional ultrasound wave field. A two-dimensional incident standing ultrasound wave field with (a) pressure amplitude $|p|$ (color), (b) velocity amplitude $|\mathbf{u}|$ (color), and (c)-(d) acoustic radiation force (quiver) that drives particles (circles) to the steady-state positions, where the acoustic radiation potential U (green) is locally minimum, which corresponds to (c) the nodes or (d) the antinodes of the incident ultrasound wave field, based on the sign of the acoustic contrast factor Φ.

particles (circles) in a 2D standing ultrasound wave with (a) pressure amplitude $|p|$ and (b) velocity amplitude $|\mathbf{u}|$, generated by two pairs of ultrasound transducers. Figure 1.10(c) and (d) show the acoustic radiation potential U (green) corresponding to the case of $\Phi > 0$ (Fig. 1.10(c)) and $\Phi < 0$ (Fig. 1.10(d)), which results in acoustic radiation force $\mathbf{f}$ (quiver) that drives the particles (circles) to the steady-state positions, where U is locally minimum. Thus, by controlling the nodes of the standing ultrasound wave, ultrasound directed self-assembly enables organizing user-specified patterns of particles, or manipulating particles throughout the reservoir.

1.4.3 Ultrasound directed self-assembly applications

In this dissertation, we focus on utilizing ultrasound DSA as a manufacturing process for tailoring the microstructure of engineered materials consisting of user-specified patterns of nano- or microparticles embedded in a polymer matrix material. Additionally, ultrasound DSA finds application in a wide range of science and engineering applications. In this section, we discuss two groups of applications that have been significantly benefitted by ultrasound DSA: biomedical devices (Sec. 1.5.1), and process control (Sec. 1.5.2). However, the list of applications presented in this section is not exhaustive, and new applications of ultrasound DSA are pursued by researchers in a broad range of research fields.

1.4.3.1 *Biomedical devices*

The biomedical community actively pursues ultrasound DSA for lab-on-a-chip applications including cell sorting [1.49], noninvasive bioassays [1.50], and cell-cell interaction studies [1.51]. When manipulating cells, it is critical to ensure that the cell is not damaged and that the cellular functions are not impeded. In an ultrasound wave field,

the cellular damage is caused by heat generation within the ultrasound transducers due to dielectric losses [1.52] and within the cell as it absorbs the ultrasound wave field, or due to cavitation effects, which create regions of ultrahigh pressure and fluid velocity that result in high mechanical stress in the cell [1.53]. Cellular damage can be mitigated by reducing the ultrasound wave field amplitude to maintain the temperature at biocompatible levels (< 40.5 °C for human cells), and the ultrasound wave field frequency to < 2 MHz to inhibit cavitation [1.54]. Thus, using moderate ultrasound wave field amplitudes and low ultrasound frequencies, cells can be manipulated in a noninvasive manner, which facilitates observation of cellular functions and cell-cell interactions. Figure 1.11 shows an encapsulated 3D HepG2 cell aggregate suspended in a standing ultrasound wave field (frequency 1.5 MHz and pressure amplitude 90 kPa) for (a) 0 days and (b) 3 days [1.55]. Comparing Fig. 1.11(b) to Fig. 1.11(a) it is apparent that the cells have grown, indicating their viability within the ultrasound wave field.

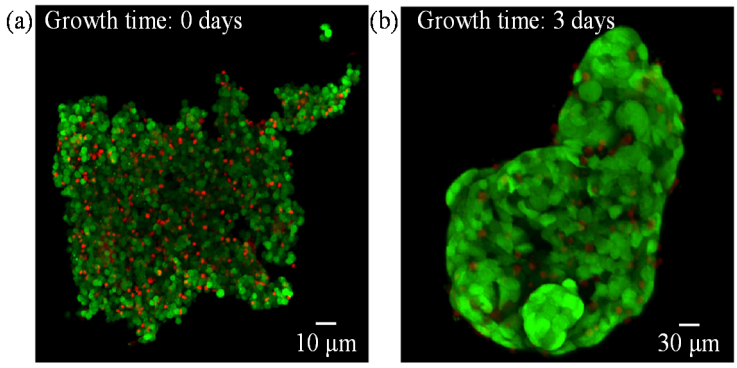

Figure 1.11: Encapsulated 3D HepG2 cell aggregate suspended in an ultrasound wave field. 3D HepG2 cell aggregate after (a) 0 days and (b) 3 days, with living cells indicated by green die [1.55]. Images adapted with permission from [1.55]. Copyright 2008 AAAS.

1.4.3.2 *Process control*

The ability to quickly sort, manipulate and/or organize user-specified patterns of nano- or microparticles is of great interest for many industrial processes including, bubble [1.56] and particle filtration [1.57], [1.58], carbon capture from coal-burning smokestacks [1.59], and 3D graphics [1.60]. Figure 1.12 shows an illustration of the filtration process using ultrasound DSA. A particle/fluid medium mixture enters the filtration device from the left and passes through an ultrasound transducer (red). The ultrasound transducer generates a standing ultrasound wave field, which drives the particles to either the node(s) or antinode(s) of the wave field, depending on the density Φ_ρ and compressibility contrast factors Φ_β. Figure 1.12 depicts the case where Φ_ρ and $\Phi_\beta > 0$, which corresponds to particles that are denser and less compressible than the fluid medium and, thus, collect at the node of the ultrasound wave field. Once the particles are driven to the node of the ultrasound wave field, the filtration device separates into multiple channels, where the center channel contains a high concentration of particles, and the other channels contain pure fluid medium.

Effective particle filtering is dependent on several limiting factors including the

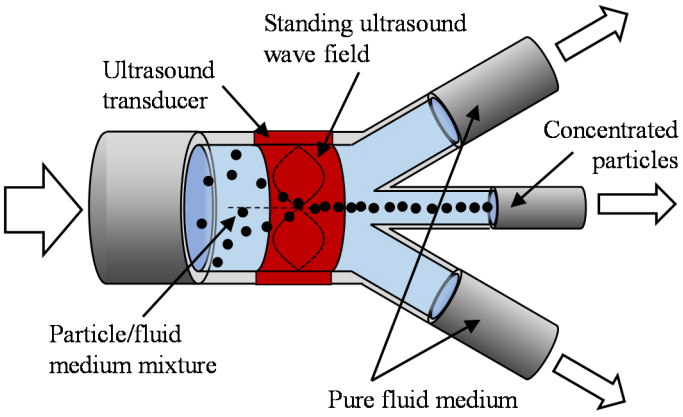

Figure 1.12: Particle filtration via ultrasound directed self-assembly. Illustration of the process for filtering particles out of a fluid medium via ultrasound directed self-assembly to purify the fluid medium and/or concentrate the particles in a dilute particle/fluid medium mixture.

material properties of the particles and fluid, the particle size, and the frequency and amplitude of the ultrasound wave field. From Eqs. (1.3) - (1.6), we find a decrease in the acoustic radiation force amplitude for small particle radii r_p, or when the particle/fluid medium has similar density ($\rho_p \approx \rho_f$) or compressibility ($\beta_p \approx \beta_f$). To mitigate these effects and ensure that the particles are driven to the node of the ultrasound wave field, we can increase the amplitude and/or frequency of the ultrasound wave field. However, increasing the ultrasound wave field amplitude and frequency requires additional power and, thus, decreases the economic feasibility of the particle filtering technique [1.59].

1.5 Dissertation structure

This dissertation is organized as follows. We first model the dynamics of a spherical particle in a standing ultrasound wave field and analyze its motion as it is driven to either the node or antinode of the standing ultrasound wave field (Ch. 2). We then implement ultrasound DSA to control the positions of the ultrasound wave field nodes and antinodes, which enables manipulating particles and organizing them into user-specified patterns in 1D (Ch. 3) and 2D (Ch. 4). Finally, we integrate ultrasound DSA with SLA as a manufacturing process to enable 3D printing macroscale engineered materials consisting of a polymer matrix with a user-specified microstructure consisting of a pattern of particles.

1.6 References

[1.1] Z. G. Nicolaou and A. E. Motter, "Mechanical metamaterials with negative compressibility transitions," *Nat. Mater*. vol. 11, pp. 608–613, 2012.

[1.2] M. H. Al-Saleh and U. Sundararaj, "A review of vapor grown carbon nanofiber/polymer conductive composites," *Carbon*, vol. 47, pp. 2–22, 2009.

[1.3] S. J. Corbitt, M. Francoeur, and B. Raeymaekers, "Implementation of optical dielectric metamaterials: A review," *J. Quant. Spectrosc. Radiat. Transf.*, vol. 158, pp. 3–16, 2015.

[1.4] S. A. Cummer, J. Christensen, and A. Alù, "Controlling sound with acoustic metamaterials," *Nat. Rev. Mater.*, vol. 1, 2016.

[1.5] V. M. Shalaev, "Optical negative-index metamaterials," *Nat. Photonics*, vol. 1, pp. 41–48, 2007.

[1.6] S. Zhang, W. Fan, K. J. Malloy, S. R. J. Brueck, N. C. Panoiu, and R. M. Osgood, "Demonstration of metal-dielectric negative-index metamaterials with improved performance at optical frequencies," *JOSA B*, vol. 23, pp. 434–438, 2006.

[1.7] Y. Xie, W. Wang, H. Chen, A. Konneker, B.-I. Popa, and S. A. Cummer, "Wavefront modulation and subwavelength diffractive acoustics with an acoustic metasurface," *Nat. Commun.*, vol. 5, pp. 5553, 2014.

[1.8] W. Guo, C. Liu, X. Sun, Z. Yang, H. G. Kia, and H. Peng, "Aligned carbon nanotube/polymer composite fibers with improved mechanical strength and electrical conductivity," *J. Mater. Chem.*, vol. 22, pp. 903–908, 2012.

[1.9] D. Schurig, J. J. Mock, B. J. Justice, S. A. Cummer, J. B. Pendry, A. F. Starr, and D. R. Smith, "Metamaterial electromagnetic cloak at microwave frequencies," *Science*, vol. 314, pp. 974–977, 2006.

[1.10] S. Zhang, L. Yin, and N. Fang, "Focusing ultrasound with an acoustic metamaterial network," *Phys. Rev. Lett*., vol. 102, pp. 194301, 2009.

[1.11] X. Zhang and Z. Liu, "Superlenses to overcome the diffraction limit," *Nat. Mater*., vol. 7, pp. 435–441, 2008.

[1.12] R. Thiruvengadathan, V. Korampally, A. Ghosh, N. Chanda, K. Gangopadhyay, and S. Gangopadhyay, "Nanomaterial processing using self-assembly-bottom-up chemical and biological approaches," *Rep. Prog. Phys*., vol. 76, pp. 06650, 2013.

[1.13] M. Grzelczak, J. Vermant, E. M. Furst, and L. M. Liz-Marzán, "Directed self-assembly of nanoparticles," *ACS Nano*, vol. 4, pp. 3591–3605, 2010.

[1.14] T. D. Clark, R. Ferrigno, J. Tien, K. E. Paul, and G. M. Whitesides, "Template-directed self-assembly of 10-μ m-sized hexagonal plates," *J. Am. Chem. Soc*., vol. 124, pp. 5419–5426, 2002.

[1.15] Y. Pan, M. Gao, L. Huang, F. Liu, and H.-J. Gao, "Directed self-assembly of monodispersed platinum nanoclusters on graphene Moiré template," *Appl. Phys. Lett*., vol. 95, pp. 093106, 2009.

[1.16] Z. Nie, A. Petukhova, and E. Kumacheva, "Properties and emerging applications of self-assembled structures made from inorganic nanoparticles," *Nat. Nanotechnol*., vol. 5, pp. 15–25, 2010.

[1.17] P. Maury, M. Escalante, D. N. Reinhoudt, and J. Huskens, "Directed assembly of

nanoparticles onto polymer-imprinted or chemically patterned templates fabricated by nanoimprint lithography," *Adv. Mater*., vol. 17, pp. 2718-2723, 2005.

[1.18] E. Dujardin, C. Peet, G. Stubbs, J. N. Culver, and S. Mann, "Organization of metallic nanoparticles using tobacco mosaic virus templates," *Nano Lett*., vol. 3, pp. 413–417, 2003.

[1.19] S. B. Darling, "Directing the self-assembly of block copolymers," *Prog. Polym. Sci*., vol. 32, pp. 1152–1204, 2007.

[1.20] A. Haryono and W. H. Binder, "Controlled arrangement of nanoparticle arrays in block-copolymer domains," *Small*, vol. 2, pp. 600–611, 2006.

[1.21] Y. Chen, H. Liu, T. Ye, J. Kim, and C. Mao, "DNA-directed assembly of single-wall carbon nanotubes," *J. Am. Chem. Soc*., vol. 129, pp. 8696–8697, 2007.

[1.22] E. Dujardin, L.-B. Hsin, C. R. C. Wang, and S. Mann, "DNA-driven self-assembly of gold nanorods," *Chem. Commun*., vol. 14, pp. 1264-1265, 2001.

[1.23] M. Fialkowski, K. J. M. Bishop, R. Klajn, S. K. Smoukov, C. J. Campbell, and B. A. Grzybowski, "Principles and implementations of dissipative (dynamic) self-assembly," *J. Phys. Chem. B*, vol. 110, pp. 2482–2496, 2006.

[1.24] C.-L. Chen and N. L. Rosi, "Peptide-based methods for the preparation of nanostructured inorganic materials," *Angew. Chem. Int. Ed*., vol. 49, pp. 1924–1942, 2010.

[1.25] L. Malaquin, T. Kraus, H. Schmid, E. Delamarche, and H. Wolf, "Controlled particle placement through convective and capillary assembly," *Langmuir*, vol. 23, pp. 11513–11521, 2007.

[1.26] K. D. Hermanson, S. O. Lumsdon, J. P. Williams, E. W. Kaler, and O. D. Velev, "Dielectrophoretic assembly of electrically functional microwires from nanoparticle suspensions," *Science*, vol. 294, pp. 1082–1086, 2001.

[1.27] S. K. Smoukov, S. Gangwal, M. Marquez, and O. D. Velev, "Reconfigurable responsive structures assembled from magnetic Janus particles," *Soft Matter*, vol. 5, pp. 1285, 2009.

[1.28] B. Raeymaekers, C. Pantea, and D. N. Sinha, "Manipulation of diamond nanoparticles using bulk acoustic waves," *J. Appl. Phys*. vol. 109, pp. 014317, 2011.

[1.29] C. R. P. Courtney, C.-K. Ong, B. W. Drinkwater, A. L. Bernassau, P. D. Wilcox, and D. R. S. Cumming, "Manipulation of particles in two dimensions using phase controllable ultrasonic standing waves," *Proc. R. Soc. A*, vol. 468, pp. 337–360, 2012.

[1.30] J. Greenhall, F. Guevara Vasquez, and B. Raeymaekers, "Ultrasound directed self-assembly of user-specified patterns of nanoparticles dispersed in a fluid medium," *Appl. Phys. Lett*., vol. 108, pp. 103103, 2016.

[1.31] M. Prisbrey, J. Greenhall, F. Guevara Vasquez, and B. Raeymaekers, "Ultrasound directed self-assembly of three-dimensional user-specified patterns of particles in a fluid medium," *J. Appl. Phys*., vol. 121, pp. 014302, 2017.

[1.32] L. E. Kinsler, A. R. Frey, A. B. Coppens, and J. V. Sanders, *Fundamentals of Acoustics*, NJ, USA: John Wiley, 2000.

[1.33] N. Asmar, in *Partial Differential Equations and Boundary Value Problems with Fourier Series*, NJ, USA: Pearson Education, 2004, pp. 173.

[1.34] A. Grinenko, P. D. Wilcox, C. R. P. Courtney, and B. W. Drinkwater, "Proof of principle study of ultrasonic particle manipulation by a circular array device," *Proc. R. Soc. A*, vol. 468, pp. 3571–3586, 2012.

[1.35] L. C. Wrobel, *The Boundary Element Method, Applications in Thermo Fluids and Acoustics,* NJ, USA: John Wiley & Sons, 2002.

[1.36] J.-F. Sigrist, *Fluid-Structure Interaction*, NJ, USA: John Wiley & Sons, 2015.

[1.37] Lord Rayleigh, *The Theory of Sound*, NY, USA: Dover Publications, 1945.

[1.38] Philip M. Morse, *Vibration and Sound* MI, USA: American Inst. of Physics, 1981.

[1.39] J. J. Faran, “Sound scattering by solid cylinders and spheres,” *J. Acoust. Soc. Am*., vol. 23, pp. 405–418, 1951.

[1.40] X. Chen and R. E. Apfel, "Radiation force on a spherical object in an axisymmetric wave field and its application to the calibration of high-frequency transducers," *J. Acoust. Soc. Am*., vol. 99, pp. 713–724, 1996.

[1.41] D. N. Cheeke, in *Fundamentals and Applications of Ultrasonic Waves*, FL, USA: CRC Press, 2002, pp. 104–138.

[1.42] L. P. Gor’kov, "On the forces acting on a small particle in an acoustical field in an ideal fluid," *Sov. Phys. Dokl*., vol. 6, pp. 773–775, 1962.

[1.43] L. V. King, "On the acoustic radiation pressure on spheres," *Proc. R. Soc. Lond. Math. Phys. Eng. Sci*., vol. 147, pp. 212–240, 1934.

[1.44] C. Eckart, "Vortices and streams caused by sound waves," *Phys. Rev*., vol. 73, pp. 68–76, 1948.

[1.45] P. J. Westervelt, "The theory of steady forces caused by sound waves," *J. Acoust. Soc. Am*., vol. 23, pp. 312–315, 1951.

[1.46] M. Barmatz and P. Collas, "Acoustic radiation potential on a sphere in plane, cylindrical, and spherical standing wave fields," *J. Acoust. Soc. Am*., vol. 77, pp. 928–945, 1985.

[1.47] O. A. Sapozhnikov and M. R. Bailey, "Radiation force of an arbitrary acoustic beam on an elastic sphere in a fluid," *J. Acoust. Soc. Am*., 133, vol. 661–676 2013.

[1.48] J. Greenhall, F. Guevara Vasquez, and B. Raeymaekers, "Dynamic behavior of microscale particles controlled by standing bulk acoustic waves," *Appl. Phys. Lett*., vol. 105, pp. 144105, 2014.

[1.49] L. Ren, Y. Chen, P. Li, Z. Mao, P.-H. Huang, J. Rufo, F. Guo, L. Wang, J. P. McCoy, S. J. Levine, and T. J. Huang, "A high-throughput acoustic cell sorter," *Lab Chip*, vol. 15, pp. 3870–3879, 2015.

[1.50] M. Evander, L. Johansson, T. Lilliehorn, J. Piskur, M. Lindvall, S. Johansson, M. Almqvist, T. Laurell, and J. Nilsson, "Noninvasive acoustic cell trapping in a microfluidic perfusion system for online bioassays," *Anal. Chem*., vol. 79, pp. 2984–2991, 2007.

[1.51] F. Guo, P. Li, J. B. French, Z. Mao, H. Zhao, S. Li, N. Nama, J. R. Fick, S. J. Benkovic, and T. J. Huang, "Controlling cell–cell interactions using surface acoustic waves," *Proc. Natl. Acad. Sci*., vol. 112, pp. 43–48, 2015.

[1.52] X. Liao, T. Jiang, Z. Huang, and S. Cochran, "Loss characterisation of piezocrystals under elevated environmental conditions," in *Applications of Ferroelectrics, European Conference on Application of Polar Dielectrics, and Piezoelectric Force Microscopy Workshop, 2016 Joint IEEE International Symposium*, 2016, pp. 1–4.

[1.53] S. B. Barnett, H.-D. Rott, G. R. ter Haar, M. C. Ziskin, and K. Maeda, "The sensitivity of biological tissue to ultrasound," *Ultrasound Med. Biol*., vol. 23, pp. 805–812, 1997.

[1.54] M. Wiklund, "Acoustofluidics 12: Biocompatibility and cell viability in microfluidic acoustic resonators," *Lab. Chip*, vol. 12, pp. 2018–2028, 2012.

[1.55] D. Bazou, W. T. Coakley, A. J. Hayes, and S. K. Jackson, "Long-term viability and proliferation of alginate-encapsulated 3-D HepG2 aggregates formed in an ultrasound trap," *Toxicol. In Vitro*, vol. 22, pp. 1321–1331, 2008.

[1.56] E. H. Trinh, D. D. Elleman, and T. G. Wang, "Acoustic bubble removal method," U.S. Patent 4 398 925, August 16, 1983.

[1.57] B. Jung, K. Fisher, K. D. Ness, K. A. Rose, and R. P. Mariella, "Acoustic particle filter with adjustable effective pore size for automated sample preparation," *Anal. Chem*., vol. 80, pp. 8447–8452, 2008.

[1.58] C. Lee, J. Lee, H. Ham Kim, S.-Y. Teh, A. Lee, I.-Y. Chung, J. Yeong Park, and

K. Kirk Shung, "Microfluidic droplet sorting with a high frequency ultrasound beam," *Lab. Chip*, vol. 12, pp. 2736–2742, 2012.

[1.59] D. Karpul, J. Tapson, M. Rapson, A. Jongens, and G. Cohen, "Limiting factors in acoustic separation of carbon particles in air," J. *Acoust. Soc. Am*., vol. 127, pp. 2153–2158, 2010.

[1.60] Y. Ochiai, T. Hoshi, and J. Rekimoto, "Pixie dust: graphics generated by levitated and animated objects in computational acoustic-potential field," *ACM Trans. Graph*., vol. 33, pp. 1–13, 2014.

CHAPTER 2

DYNAMIC BEHAVIOR OF A MICROSCALE PARTICLE IN AN ULTRASOUND WAVE FIELD

Adapted with permission from J. Greenhall, F. Guevara Vasquez, and B. Raeymaekers, "Dynamic behavior of microscale particles controlled by standing bulk acoustic waves," Appl. Phys. Lett. **105** 144105 (2014).

2.1 Introduction

In this chapter, we address the first objective of this dissertation by deriving a model for the dynamics of a single spherical particle in a fluid medium subject to a one-dimensional ultrasound wave field. We analyze the transient and steady-state behavior of the particle submerged in a fluid medium, driven to the node of a standing ultrasound wave field created by two opposing ultrasound transducers. We derive the dynamics of the fluid-particle system taking into account the acoustic radiation force and the time-dependent and time-independent drag force acting on the particle. Using this model, we characterize the transient and steady-state behavior of the fluid-particle system as a function of the particle and fluid medium properties and the ultrasound transducer operating parameters.

2.2 Theoretical model

Figure 2.1 shows a schematic of a one-dimensional (1D) reservoir of length L with opposing ultrasound transducers that contains a fluid medium with one particle of radius r_p, initially located at a node of a standing ultrasound wave field $\varphi(X,t)$. At $t = 0$, a step input to the ultrasound transducer phases displaces the node over a distance smaller than $\lambda/4$ [2.1]–[2.3]. This exposes the particle to a non-zero acoustic radiation force, driving it

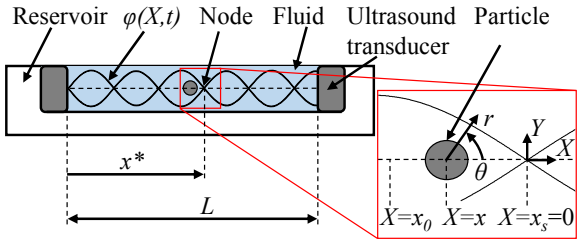

Figure 2.1: Schematic of a one-dimensional fluid reservoir. Cross-sectional view of a fluid reservoir with two opposing ultrasound transducers, creating a standing acoustic wave $\varphi(X,t)$. The inset image shows a magnified view of the particle located at $X = x$, with respect to the node to which it is driven, located at $X = x_s$. The initial position of the particle $X = x_0$ and the spherical coordinates (r, θ) originating at the center of the particle are defined.

from its initial position x_0 towards the new steady-state node located at x_s, expressed in a local Cartesian coordinate system with origin at the node to which the particle is driven ($X = x_s = 0$). Hence, the displacement of the particle $\Delta x = |x_s - x_0|$, is identical to the displacement of the node. x^* indicates the position of the node to which the particle is driven, relative to the ultrasound transducer rather than the local coordinate system. The inset of Fig. 2.1 shows the particle located at $X = x$, the initial and final positions of the particle, and the spherical coordinate system (r, θ) with origin at the center of the particle.

The dynamics of the fluid-particle system are expressed as

$$m\ddot{x} - F_r(x) - F_d(x,t) = 0\,, \tag{2.2}$$

where m is the mass and $\ddot{x} = d^2x/dt^2$ is the acceleration of the particle. F_r is the acoustic radiation force in the x-direction and F_d is the drag force acting on the particle in the x-direction. To calculate F_r and F_d, we first define the ultrasound wave field in the reservoir. The ultrasound wave field incident to the particle for the case of a standing plane ultrasound wave field is written in terms of a velocity potential as

$$\varphi(X,t) = \mathrm{Re}\left(-\varphi_0 e^{i\omega t} i\left(e^{ikX} - e^{-ikX}\right)\right), \tag{2.3}$$

where φ_0 is the amplitude of the standing ultrasound wave field, ω is the operating frequency, and $k = 2\pi/\lambda$ is the wave number. Re(·) refers to the real part of Eq. (2.3). Defining $X = r\cos\theta + x$, with x the location of the particle, Eq. (2.3) is rewritten in the spherical particle coordinate system as [2.4]

$$\varphi(r,\theta,t) = \mathrm{Re}\left(\sum_{n=0}^{\infty} A_n j_n(kr) P_n(\cos\theta)\right). \tag{2.4}$$

Here $j_n(\cdot)$ is the n^{th} order spherical Bessel function of the first kind, $P_n(\cdot)$ is the n^{th} order Legendre polynomial, and

$$A_n = -\varphi_0 e^{i\omega t}\left(e^{ikx} - (-1)^n e^{-ikx}\right)(2n+1)i^{n+1}. \tag{2.5}$$

The scattered ultrasound wave field resulting from the interaction between the ultrasound wave field and the particle is written as [2.4]–[2.6]

$$\varphi_{sc}(r,\theta,t) = \mathrm{Re}\left(\sum_{n=0}^{\infty} A_n B_n h_n(kr) P_n(\cos\theta)\right). \tag{2.6}$$

Here, $h_n(\cdot)$ is the n^{th} order Hankel function of the first kind, and $B_n = \alpha_n + i\sigma_n$ is the complex scattering coefficient calculated from the boundary conditions at the fluid-particle interface. The following conditions hold: (i) the fluid pressure is equal to the normal stress at the surface of the particle, (ii) no fluid penetration in the particle occurs, and (iii) the shear stress is zero at the surface of the particle [2.4], [2.5]. A complete derivation of the scattering coefficient B_n is given by Faran [2.4]. The resulting ultrasound wave field in the reservoir is the sum of the incident and scattered ultrasound wave field, $\varphi_{tot} = \varphi + \varphi_{sc}$. The acoustic radiation force F_r acting on the particle in the x-direction is calculated from the rate of momentum within a control volume V enclosing the particle,

$$F_r = \int_V \frac{\partial}{\partial t}\left(\rho_f \mathbf{u}\right) dV, \tag{2.7}$$

where $\mathbf{u} = -\nabla\varphi_{tot}$ is the 3D velocity vector of the fluid. Chen et al. showed that for the case of a standing plane ultrasound wave field (Eq. (2.3)) the acoustic radiation force acting on a spherical particle in the direction of wave propagation (x-direction) is written as [2.5]

$$F_r = -C_r \sin 2kx \,, \tag{2.8}$$

with

$$C_r = 4\rho_f \pi \left|\varphi_0\right|^2 \sum_{n=0}^{\infty} \left(-\sigma_n + \sigma_{n+1} + 2\alpha_n \sigma_{n+1} - 2\sigma_n \alpha_{n+1}\right). \tag{2.9}$$

Since $r_p \ll \lambda$ (Rayleigh regime), Eq. (2.9) can be approximated by its low-frequency expansion [2.5]

$$C_r = 4\rho_f \pi \left|\varphi_0\right|^2 \left(\Phi\left(kr_p\right)^3 + O\left(kr_p\right)^5\right), \tag{2.10}$$

where $O(kr_p)^5$ represents the fifth and higher order terms. In addition, Westervelt showed that a particle in a standing ultrasound wave field is subject to Stokes and Oseen forces, i.e., the drag force on the particle caused by velocity difference between the particle surface and the surrounding fluid medium, given as [2.7]

$$F_d = C_s\left(\bar{u} - \dot{x}\right) + C_o\left(\bar{u} - \dot{x}\right)\left|\bar{u} - \dot{x}\right|. \tag{2.11}$$

Here $\dot{x} = dx/dt$ is the particle velocity, $C_s = 6\pi\mu_f r_p$ and $C_o = 9/4\pi\rho_f r_p^2$ are the Stokes and Oseen coefficients, respectively, and μ_f is the dynamic viscosity of the fluid medium. $\bar{u}$ is the fluid velocity at the particle surface in the X-direction, averaged over $\theta \in [0, \pi]$, i.e.,

$$\bar{u} = -\frac{1}{\pi}\int_0^{\pi}\left(\frac{\partial \varphi_{tot}}{\partial r}\cos\theta - \frac{1}{r_p}\frac{\partial \varphi_{tot}}{\partial \theta}\sin\theta\right)d\theta \,. \tag{2.12}$$

Thus, using $\varphi_{tot} = \varphi + \varphi_{sc}$ and Eqs. (2.4) and (2.6) we find that

$$\bar{u}(t) = \mathrm{Re}\left(u_0 e^{i\omega t}\cos kx\right), \tag{2.13}$$

where x is the position of the particle and u_0 is the fluid velocity amplitude, i.e.,

$$u_0 = \mathrm{Re}\left(-\frac{\varphi_0}{\pi}\sum_{n=0}^{\infty} A_n G_n \left\{k\left(j_n'\left(kr_p\right) + B_n h_n'\left(kr_p\right)\right) + \frac{1}{r_p}\left(j_n\left(kr_p\right) + B_n h_n\left(kr_p\right)\right)\right\}\right). \tag{2.14}$$

The prime denotes the first derivative of $j_n(\cdot)$ and $h_n(\cdot)$ with respect to kr_p. G_n is defined as

$$G_n = \begin{cases} 0 & \text{, even } n \\ \dfrac{\Gamma(n/2)\Gamma(n/2+1)}{((n-1)/2)!((n+1)/2)!} & \text{, odd } n, \end{cases} \tag{2.15}$$

where $\Gamma(\cdot)$ is the Gamma function. Combining Eqs. (2.2) and (2.9) - (2.16) yields the dynamics of the fluid-particle system

$$m\ddot{x} + C_r \sin 2kx - C_s\left(\bar{u} - \dot{x}\right) - C_o\left(\bar{u} - \dot{x}\right)\left|\bar{u} - \dot{x}\right| = 0\,. \tag{2.16}$$

Assuming small fluid velocity amplitude u_0 and particle displacement Δx, we linearize Eq. (2.16), i.e.,

$$\ddot{x} + 2\zeta\omega_n\dot{x} + \omega_n^2 x - C_s\bar{u} = 0\,, \tag{2.17}$$

with the damping coefficient $\zeta = C_s / \sqrt{8kmC_r}$, and the natural frequency $\omega_n = \sqrt{2kC_r / m}$. Increasing the amplitude of the standing ultrasound wave field φ_0 increases the fluid velocity amplitude u_0, causing the solution of the linearized system to diverge from that of Eq. (2.16), resulting in a nonlinear response. The particle will approach the node and then oscillate. The response of the linear system (Eq. (2.17)) can be solved given the initial conditions ($x(t=0) = x_0, \dot{x}(t=0) = 0$) and is a function of Δx. However, no closed-form

solution has been documented in the literature describing the response of the nonlinear system (Eq. (2.16)). Hence, we numerically simulate the trajectory of a particle while it is driven to the node of the standing ultrasound wave field using a second order Runge-Kutta scheme.

Eq. (2.16) shows that the particle trajectory is defined by a time-independent acoustic radiation force that drives the particle towards the node, and a time-independent Stokes drag force and time-dependent Stokes and Oseen drag forces that resist the particle motion. Once the particle reaches the node of the standing ultrasound wave field, the amplitude of the radiation force and the average velocity of the particle is zero, causing the time-independent Stokes drag force to be zero. Thus, the time-dependent Stokes and Oseen drag force and the particle inertia dominate the dynamics of the fluid-particle system and the particle enters into a stable periodic oscillation with amplitude $\tilde{x}$ around the node. Because the time-dependent terms in Eq. (2.16) are oscillatory and quasi-reversible over one period T of the standing ultrasound wave field, their effect on the average position of the particle over T is negligible, and the average particle position is dictated by the time-independent radiation force F_r and time-independent Stokes drag force $C_s\dot{x}$. We define the nondimensional variable K_1 as the ratio of the maximum acoustic radiation force that the particle can experience, i.e., when it is located halfway between the node and antinode, and the maximum possible time-independent Stokes drag force, i.e., the drag force when the particle travels at c_f. Hence,

$$K_1 = \frac{\rho_f \varphi_0^2 \Phi \left(kr_p\right)^3}{\mu r_p c_f}. \tag{2.18}$$

Adjusting K_1 simultaneously changes ω_n and ζ as $K_1 \sim \omega_n^2$ and $K_1 \sim 1/\zeta^2$. In most applications, it is necessary for a particle to be stationary at a desired location and to minimize oscillation amplitude $\tilde{x}$ around the desired location. To characterize $\tilde{x}$ we define the dimensionless variable K_2 as the ratio of the time-dependent Stokes and Oseen drag forces and the particle inertia for the maximum steady-state particle velocity $\dot{x} = -\bar{u}$. Hence,

$$K_2 = \frac{\mu + \varphi_0 \rho_f k r_p}{\omega \rho_p r_p^{\,2}} . \tag{2.19}$$

The transient and steady-state response of the system is controlled by altering the forces acting on the particle, through adjustment of K_1 and K_2. The transient response is characterized by the settling time T_s and the percent overshoot M_p, whereas the steady-state behavior is characterized by the oscillation amplitude $\tilde{x}$ of the particle around the node of the standing ultrasound wave field. We define T_s as the time for which the average position of the particle over one period of the ultrasound wave field remains within $x_s \pm 0.01\Delta x$, and the percent overshoot M_p as the ratio of the maximum particle overshoot beyond $x = x_s$ and λ.

2.3 Dynamic response of a spherical particle in an ultrasound wave field

Figures 2.2(a), (b) and (c) show the nondimensional settling time, the percent overshoot, and the nondimensional oscillation amplitude, each as a function of K_1, for $\Phi_1 = 0.74$, $\Phi_2 = 0.12$, and $\Phi_3 = -27.56$, which represent a 304 stainless steel, polystyrene, and cork particle in water, respectively. The results are shown for $\Delta x = \lambda/10$. However, T_s, M_p, and $\tilde{x}$ are almost independent Δx. From Figs. 2.2(a) and (b) we observe that the settling

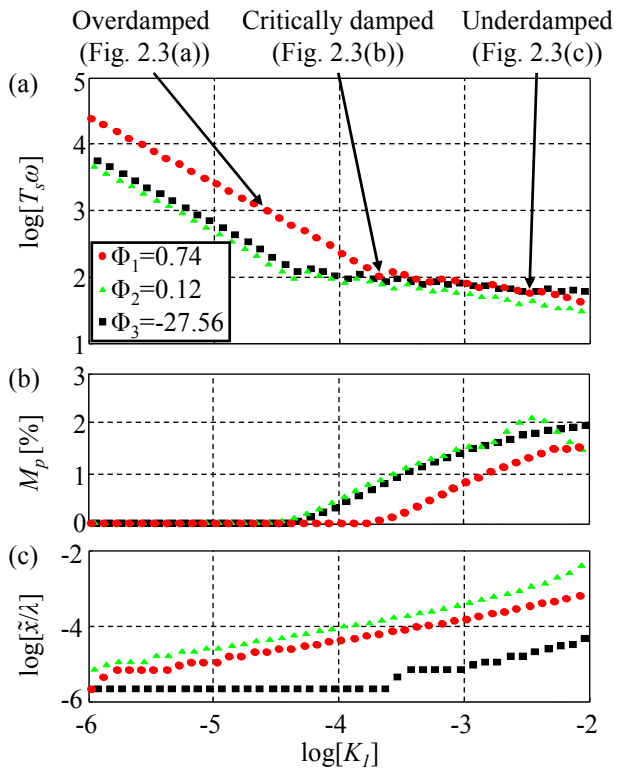

Figure 2.2: Dynamic characteristics of a spherical particle in an ultrasound wave field. (a) Nondimensional settling time, (b) percent overshoot and (c) nondimensional oscillation amplitude, as a function of K_1, for $\Phi_1 = 0.74$, $\Phi_2 = 0.12$ and $\Phi_3 = -27.56$, and for $\Delta x = \lambda/10$.

time decreases with increasing K_1 in the overdamped region, while M_p remains zero. The radiation force is small relative to the time-independent Stokes drag force, causing the particle to approach the node slowly, without overshooting it. Increasing K_1 either increases the magnitude of the acoustic radiation force or reduces the time-independent Stokes drag force. This increases the particle velocity as it travels to the node, thus reducing T_s while maintaining $M_p = 0$. Alternatively, in the underdamped region, the magnitude of the acoustic radiation force is large compared to the time-independent Stokes drag force which causes the particle to overshoot and then oscillate around the node until settling into the steady-state periodic oscillation. Increasing K_1 and, thus, the acoustic radiation force compared to the time-independent Stokes drag force drives the particle further past the node, increasing M_p while T_s remains constant. While for a second order linear system T_s

should remain strictly constant in the underdamped region, Fig. 2.2(a) indicates a slight decrease in T_s with increasing K_1. As K_1 increases within the underdamped region, the natural frequency of the fluid-particle system ω_n approaches the operating frequency ω, used to calculate the time averaged particle position. As a result, the time-averaging covers a full period of the harmonic response, filtering out the overshoots and undershoots, and causing the settling time to decrease. From Fig. 2.2(c) we observe that $\tilde{x}$ increases with K_1, as expected for a harmonically forced linear system (Eq. (2.17)). As K_1 increases, ω_n increases and approaches the operating frequency ω, which results in resonance as the particle absorbs more energy from the oscillating fluid medium. Hence, increasing K_1 results in a faster particle displacement, at the cost of increasing M_p and $\tilde{x}$.

Figure 2.3 shows typical particle trajectories $x(t)$ for the (a) overdamped, (b) critically damped, (c) underdamped, and (d) nonlinear cases, for a 304 stainless steel sphere in water

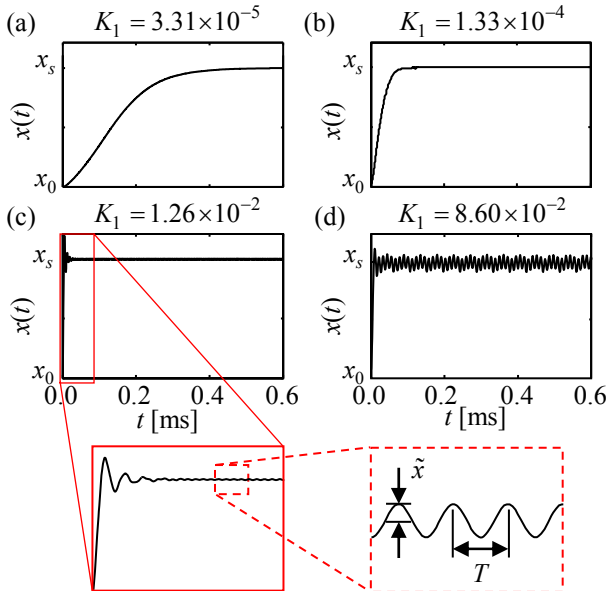

Figure 2.3: Trajectory of a spherical particle in an ultrasound wave field. Typical trajectories of a SS304 sphere submerged in water ($\Phi_1 = 0.74$) as a function of time, for $\Delta x = \lambda/10$ and $\omega = 2.10\cdot10^6$ rad/s, and for different values of K_1, corresponding to different response regimes: (a) overdamped, (b) critically damped, (c) underdamped, and (d) nonlinear. The solid-line insert shows an enlarged view of the harmonic underdamped oscillations as the position settles to the node. The dashed-line insert shows the steady-state oscillations of amplitude $\tilde{x}$ around the node, with period T.

(Φ_1 = 0.74), and for $\Delta x = \lambda/10$ and ω = 2.10·10^6 rad/s. The solid-line inset shows a magnified section of the underdamped response, illustrating the harmonic oscillations while the average position of the particle approaches the desired node position. The dashed-line inset shows an enlarged view of the particle trajectory, after it settles into the steady-state oscillation around the node of the standing ultrasound wave field. We observe the steady-state oscillations of the particle due to the oscillating fluid velocity, which applies drag force to the particle surface (see Eq. (2.11)). In the dashed-line inset, the response is underdamped, and the linear terms in the forcing function dominate, resulting in particle oscillations at the operating frequency ω. Alternatively, the nonlinear response, illustrated in Fig. 2.3(d) and obtained for high values of K_1, consists of steady-state oscillations vibrating at multiple frequencies, including ω and its higher harmonic frequencies.

Figure 2.4 shows the nondimensional amplitude of the steady-state particle oscillation as a function of K_2, which is the ratio of the total time-dependent drag force (Stokes and Oseen) that drives the particle oscillation, and the particle inertia that resists the oscillation. For small values of K_2 the fluid-particle system behaves linearly. Increasing K_2 increases

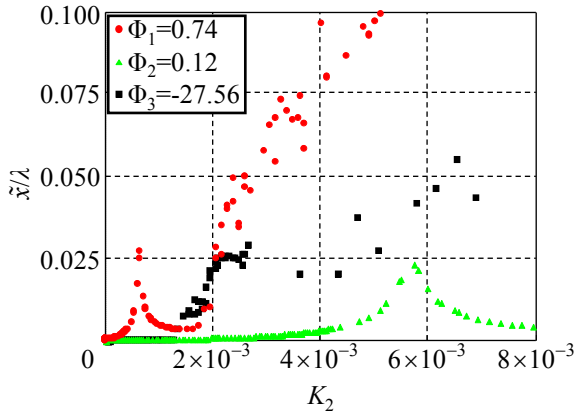

Figure 2.4: Nondimensional steady-state oscillation amplitude of a spherical particle in an ultrasound wave field. Nondimensional steady-state oscillation amplitude as a function of K_2, for Φ_1 = 0.74, Φ_2 = 0.12 and Φ_3 = -27.56.

the amplitude of the standing ultrasound wave field φ_0, which in turn increases the amplitude of the fluid velocity, thereby increasing the drag force acting on the particle and increasing the natural frequency ω_n of the system. As ω_n approaches the operating frequency ω of the standing ultrasound wave field, the system approaches resonance, which increases the steady-state oscillation amplitude. Increasing K_2 further reduces the oscillation amplitude because ω_n diverges from ω. For large values of K_2, and therefore large velocity differences between the particle and surrounding fluid medium, the time-dependent Oseen drag force dominates the total time-dependent drag force (Eq. (2.10)), resulting in nonlinear behavior of the fluid-particle system. Rather than oscillating at a single frequency, the particle oscillates at multiple frequencies (Fig. 2.3(d)), the amplitude of which increases with increasing K_2.

2.4 Conclusion

In conclusion, we have analyzed the dynamics of a particle submerged in a fluid medium, driven to the node of a standing bulk ultrasound wave field by an acoustic radiation force. We have simulated the particle trajectory, and have characterized the transient and steady-state behavior of the fluid-particle system, as a function of the particle and fluid properties and the operating parameters of the ultrasound transducers. When the dynamic behavior of the fluid-particle system is overdamped, the settling time decreases and the percent overshoot remains zero, with increasing ratio of acoustic radiation force and time-independent Stokes drag force (K_1). When the dynamic behavior of the fluid-particle system is underdamped, the settling time is constant while the percent overshoot increases with increasing K_1. We find that the particle oscillates around the node of the acoustic standing ultrasound wave field. Near the node, the amplitude of these oscillations

and the natural frequency of the fluid-particle system ω_n are dependent on the ratio of the time-dependent Stokes and Oseen damping forces and the particle inertia (K_2). For small K_2, the fluid-particle system behaves linearly, oscillating at the operating frequency ω, and resonating as the natural frequency of the system approaches ω. However, for large K_2 the system behaved nonlinearly, oscillating at multiple frequencies, including the operating frequency as well as its higher order harmonics.

2.5 References

[2.1] J. Greenhall, F. Guevara Vasquez, and B. Raeymaekers, "Continuous and unconstrained manipulation of micro-particles using phase-control of bulk acoustic waves," *Appl. Phys. Lett*., vol. 103, pp. 074103, 2013.

[2.2] C. R. P. Courtney, C.-K. Ong, B. W. Drinkwater, A. L. Bernassau, P. D. Wilcox, and D. R. S. Cumming, "Manipulation of particles in two dimensions using phase controllable ultrasonic standing waves," *Proc. R. Soc. Math. Phys. Eng. Sci*., vol. 468, pp. 337–360, 2012.

[2.3] A. Grinenko, C. K. Ong, C. R. P. Courtney, P. D. Wilcox, and B. W. Drinkwater, "Efficient counter-propagating wave acoustic micro-particle manipulation," *Appl. Phys. Lett*., vol. 101, pp. 233501, 2012.

[2.4] J. J. Faran, "Sound scattering by solid cylinders and spheres," *J. Acoust. Soc. Am*., vol. 23, pp. 405–418, 1951.

[2.5] X. Chen and R. E. Apfel, "Radiation force on a spherical object in an axisymmetric wave field and its application to the calibration of high-frequency transducers," *J. Acoust. Soc. Am*., vol. 99, pp. 713–724, 1996.

[2.6] O. A. Sapozhnikov and M. R. Bailey, "Radiation force of an arbitrary acoustic beam on an elastic sphere in a fluid," *J. Acoust. Soc. Am*., vol. 133, pp. 661–676, 2013.

[2.7] P. J. Westervelt, "The theory of steady forces caused by sound waves," *J. Acoust. Soc. Am*., vol. 23, pp. 312–315, 1951.

CHAPTER 3

ULTRASOUND DIRECTED SELF-ASSEMBLY IN ONE DIMENSION

3.1 Introduction

In this chapter, we address the second objective of the dissertation by introducing a technique for performing ultrasound directed self-assembly (DSA) to manipulate a single spherical particle in one dimension. Ultrasound DSA enables manipulating particles into user-specified positions and configurations using the acoustic radiation force that is associated with a standing ultrasound wave field (see Sec. 1.4.2) [3.1]. In a one-dimensional (1D) standing ultrasound wave field, the acoustic contrast factor Φ determines whether particles accumulate at the nodes ($\Phi > 0$) or antinodes ($\Phi < 0$) of the standing ultrasound wave field (see Sec. 1.4.2.3) [3.2]. Controlling the position of the nodes and antinodes enables manipulation of particles trapped at the nodes to a predetermined location in the fluid reservoir. This is commonly achieved through use of ultrasound transducer arrays [3.3]–[3.7]. In this work, we focus on the phase-adjustable ultrasound transducer array technique with counter-propagating wave patterns [3.5]–[3.7].

A common technique for controlling the positions of the ultrasound wave field nodes is to remove reflected waves from the reservoir, resulting in an ultrasound wave field φ that is comprised of two opposing traveling ultrasound waves φ_L and φ_R. Figure 3.1 shows three different techniques used to eliminate reflected waves within a 1D reservoir. Courtney et al. attached absorbing and backing layers to opposing piezoelectric ultrasound transducers to absorb incoming waves and reduce reflections (Fig. 3.1(a)) [3.6], [3.7]. Using the phase difference between the two ultrasound transducers, in the absence of reflections, they state that particles can be displaced across multiple wavelengths, and experimental data show displacement of particles over a half wavelength. This method requires precise implementation of the absorbing and backing layers with thicknesses of t_a and t_b,

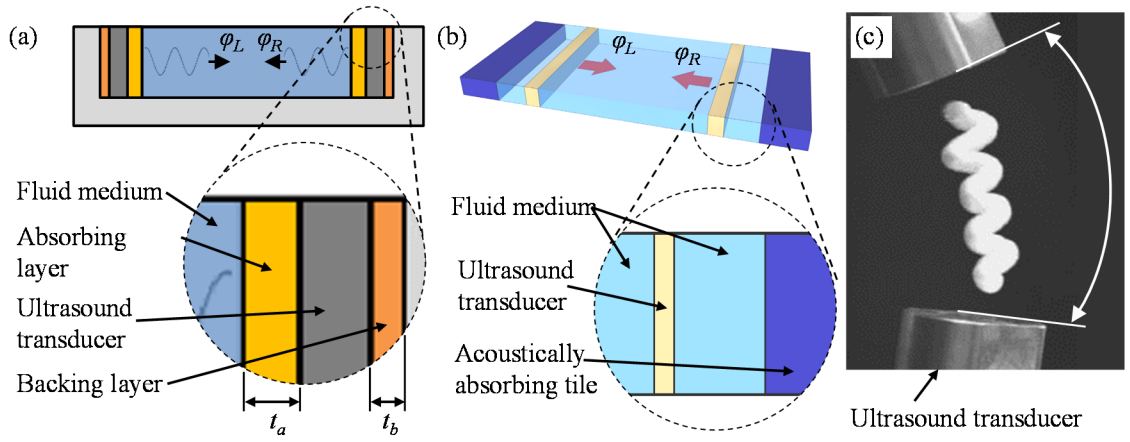

Figure 3.1: 1D ultrasound directed self-assembly techniques based on eliminating all reflected ultrasound waves. Reflected ultrasound waves are eliminated through use of (a) absorbing and backing layers with precise thicknesses t_a and t_b, respectively, [3.6] (b) a water layer and acoustically absorbing tile [3.8], and (c) angled ultrasound transducers [3.5]. Images adapted with permission from the references as indicated: (b) Copyright 2012 AIP Publishing LLC; (c) Copyright 2007 The Japan Society of Applied Physics.

respectively, to suppress reflected ultrasound waves. Grinenko et al. alleviated this problem by backing the ultrasound transducers with a fluid layer and then an acoustically absorbing tile (Fig. 3.1(b)) [3.8]. Alternatively, Kozuka et al. employed two ultrasound transducers arranged at 150° and operated at 39.6 kHz to generate a standing ultrasound wave field in air without reflections (Fig. 3.1(c)) [3.5]. They fixate a 3 mm polystyrene sphere in the antinode of the ultrasound wave field, and showed that the sphere moved almost linearly with increasing phase difference between the two ultrasound transducers.

The methods described in the literature to manipulate particles fixated at the nodes of an ultrasound wave field are derived under the assumption that no reflected ultrasound waves normal to the ultrasound transducer surface exist. This results in a straightforward solution of the wave equation, but it also requires removing those reflections in practical implementations, either by creating a backing or acoustic absorption layer, or by arranging the ultrasound transducers in an inclined orientation. Furthermore, no explicit

demonstration seems to exist of manipulating a particle over multiple wavelengths using bulk acoustic waves (including reflections). Here, we describe an alternative method, based on a solution of the wave equation that incorporates reflected ultrasound waves, thus avoiding the need for complex practical implementations. The method requires independent adjustment of the phases of two opposing ultrasound transducers, and enables unconstrained, continuous manipulation of particles dispersed in a fluid medium over multiple wavelengths, in the presence of reflected ultrasound waves. A theoretical analysis and experimental validation is presented.

3.2 Steady-state particle position

Figure 3.2 shows the cross-section of a fluid reservoir of length L with two opposing ultrasound transducers. The ultrasound wave field $\varphi(x,t)$ generated by the ultrasound transducers is described by the one-dimensional (1D) inviscid wave equation [3.9]

$$\frac{\partial^2 \varphi}{\partial x^2} + k^2 \varphi = 0, \tag{3.1}$$

where x is the direction of ultrasound wave propagation and k is the wave number. Assuming rigid ultrasound transducer surfaces, the boundary condition at the fluid-ultrasound transducer interface is derived from the impedance boundary condition (Eq.

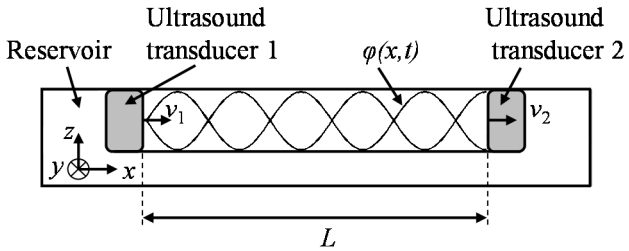

Figure 3.2: Schematic of a one-dimensional fluid reservoir. Cross-sectional view of a fluid reservoir with two opposing ultrasound transducers creating a standing ultrasound wave field $\varphi(x, t)$.

(1.2)) for rigid ultrasound transducers $\left(\tilde{Z} \approx 0\right)$ as

$$\mathbf{n} \bullet \nabla \varphi = v_j, \tag{3.2}$$

where **n** is the unit vector normal to the ultrasound transducer surface (*x*-direction, see Fig. 3.2) and v_j is the harmonic velocity amplitude of the surface of ultrasound transducer *j* (with $j \in \{1,2\}$) as it vibrates in the positive *x*-direction, given as

$$\begin{aligned} v_1 &= V_1 e^{j\psi_1} \quad \text{at } x = 0 \\ v_2 &= V_2 e^{j\psi_2} \quad \text{at } x = L. \end{aligned} \tag{3.3}$$

V_1 and V_2 are the velocity amplitudes, and ψ_1 and ψ_2 are the phases of the oscillating ultrasound transducer surfaces. In this paper, $V_1/V_2 = 1$. With these boundary conditions, the ultrasound wave field as a function of location is calculated as

$$\varphi(x) = \frac{1}{2k \sin kL}\left(V_1 e^{i\psi_1}\left(e^{ik(x-L)} + e^{-ik(x-L)}\right) - V_2 e^{i\psi_2}\left(e^{ikx} + e^{-ikx}\right)\right), \tag{3.4}$$

the real part of which is written as

$$\mathrm{Re}\left[\varphi(x)\right] = \frac{1}{k \sin kL}\left(V_1 \cos\psi_1 \cos\left(k\left(L - x\right)\right) - V_2 \cos\psi_2 \cos kx\right). \tag{3.5}$$

The location of the nodes are computed as $\mathrm{Re}[\varphi] = 0$, which yields

$$x\left(\psi_1, \psi_2\right) = \frac{1}{k}\mathrm{atan}\left(\frac{V_2 \cos\psi_2 - V_1 \cos\psi_1 \cos kL}{V_1 \cos\psi_1 \sin kL}\right) + \frac{m\pi}{k}. \tag{3.6}$$

Here, $m = 0,1,2, \ldots, n$, so that all nodal locations are contained between 0 and *L*. *n* is the number of nodes of the ultrasound wave field between the opposing ultrasound transducers.

When $k = (2n\text{-}1)\pi/2L$, for $n \in \mathbb{N}$, Eq. (3.6) is reduced to

$$x(\psi_1, \psi_2) = \frac{(-1)^{n+1}}{k} \operatorname{atan}\left(\frac{V_2 \cos\psi_2}{V_1 \cos\psi_1}\right) + \frac{m\pi}{k}. \tag{3.7}$$

Figure 3.3(a) shows the nodal locations ($x/\lambda \in [0,3]$) of the ultrasound wave field as a function of the phases of the opposing ultrasound transducers ψ_1 and ψ_2 for the case of Eq. (3.7), with $n = 48$. Only even values of m are displayed for clarity. The inset shows a section of Fig. 3.3(a) for $\psi_1, \psi_2 \in [0, \pi]$. Four example trajectories of a particle trapped in a node are indicated with a solid line. Trajectories (i) and (ii) are obtained by linearly adjusting the phase difference between the ultrasound transducers, $\Delta\psi = \psi_1 - \psi_2$ (i.e., $\Delta\psi$ (t) follows

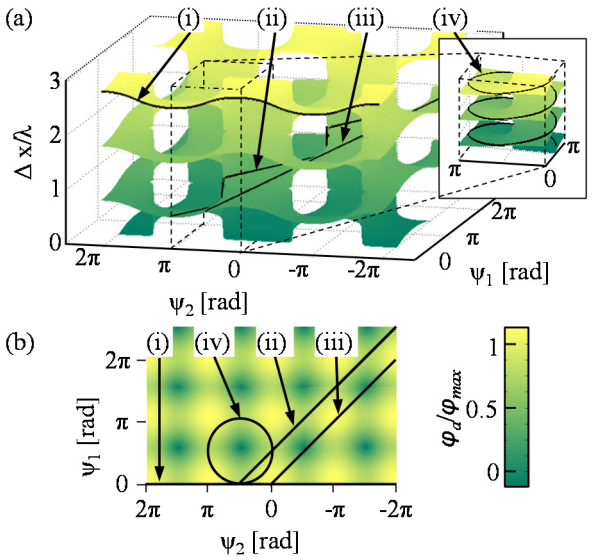

Figure 3.3. Nodal location and ultrasound wave field amplitude as a function of the ultrasound transducer phases. (a) Nodal locations of the standing ultrasound wave field, $x = \lambda$, as a function of the ultrasound transducer phases, ψ_1 and ψ_2 (for even values of m). The inset shows the section of the figure boxed with dashed lines. Four example node trajectories are shown (solid line); trajectories (i) and (ii) are based on linear adjustments of $\Delta\psi$ (t), while trajectories (iii) and (iv) are based on independent adjustments of ψ_1 and ψ_2. (b) Amplitude of the standing ultrasound wave field as a function of ψ_1 and ψ_2, identifying the same trajectories (i)–(iv) shown in (a) (solid lines), and illustrating that for certain combinations of ψ_1 and ψ_2, the amplitude of the standing ultrasound wave field approaches zero (darker), eliminating the ability to control a particle fixated in a node.

a straight line and $\Delta\psi$ (0) = 0). We observe that linear adjustment of $\Delta\psi$ will not result in displacement over multiple wavelengths. In contrast, trajectories (iii) and (iv) show that through simultaneous and independent adjustment of both ultrasound transducer phases, a particle trapped in a node can be displaced over multiple wavelengths. We assume that the ultrasound wave field satisfies the Helmholtz equation when the ultrasound transducer phases are adjusted, i.e., the transient behavior is neglected. This is an adequate approximation if the changes in the ultrasound transducer phases occur over a time scale that is significantly larger than the period of the ultrasound wave field, as is the case in our experiments. While only four trajectories resulting from specific sequences of the ultrasound transducer phases are identified, an infinite number of sequences theoretically exists (Fig. 3.3). Practically, however, particles cannot be trapped and manipulated unless the amplitude of the ultrasound wave field, $\varphi_0 > 0$. Figure 3.3 (b) shows the amplitude of the standing ultrasound wave field φ_a as a function of ψ_1 and ψ_2, normalized with the maximum possible ultrasound wave field amplitude φ_{max} for the given reservoir dimensions.

3.3 Experimental particle manipulation

Figure 3.4 shows a schematic of the experimental apparatus. It consists of a reservoir (inner dimensions: 48 × 48 × 8 mm) machined from poly(methyl methacrylate). Two ultrasound transducers (PZT type SM411) of dimensions (5 × 45 × 8 mm) and center frequency of 740 kHz are mounted on opposing walls of the reservoir. The ultrasound transducers are driven by a function generator controlled by a PC. A spherical polystyrene (PS) particle of diameter 350 μm is displaced along the *x*-direction of the reservoir over

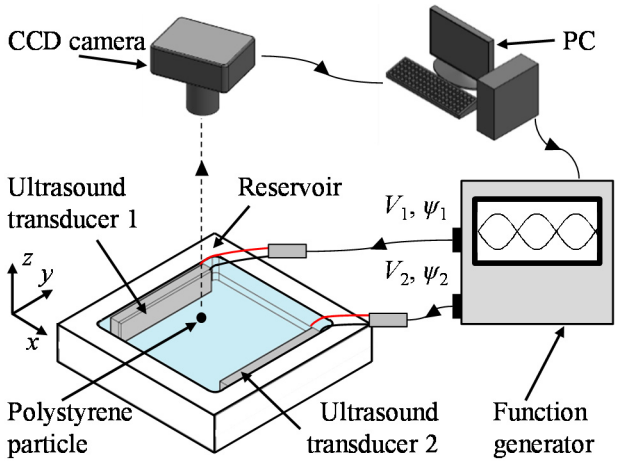

Figure 3.4: Schematic of the experimental setup. Experimental setup consisting of a water reservoir with two opposing ultrasound transducers. A spherical polystyrene particle of diameter 350 μm is neutrally buoyant in the reservoir. The ultrasound transducer phases ψ_1 and ψ_2 are adjusted by the function generator according to a specified sequence controlled by a PC, while $V_1 / V_2 = 1$. The particle is manipulated along the x-direction of the reservoir, and its displacement is captured with a CCD camera. A particle tracking algorithm is employed to quantify its position during manipulation.

two wavelengths by applying a sequence of ψ_1 and ψ_2 to the respective ultrasound transducers, as theoretically described by the solid line in the inset of Fig. 3.3 (a) (trajectory (iv)). The position of the particle is captured with a CCD camera and its displacement is quantified using a particle tracking algorithm. The fluid host medium consists of deionized water mixed with sugar to render the particle neutrally buoyant in the fluid and keep it away from the reservoir walls. The density and sound speed are ρ_p = 1062 kg/m^3 (measured), c_p = 2400 m/s for the PS particle [3.10] and ρ_f = 1062 kg/m^3 (measured), c_f = 1497 m/s (determined with time-of-flight measurement) for the fluid and, thus, the acoustic contrast factor $\Phi = 0.609$.

Figure 3.5 shows the experimental results, with (a) the sequence of ultrasound transducer phases that result in trajectory (iv) shown in the inset of Fig. 3.3 (a), (b) the theoretical (dashed) and experimental (solid) position of a particle trapped in a node of the

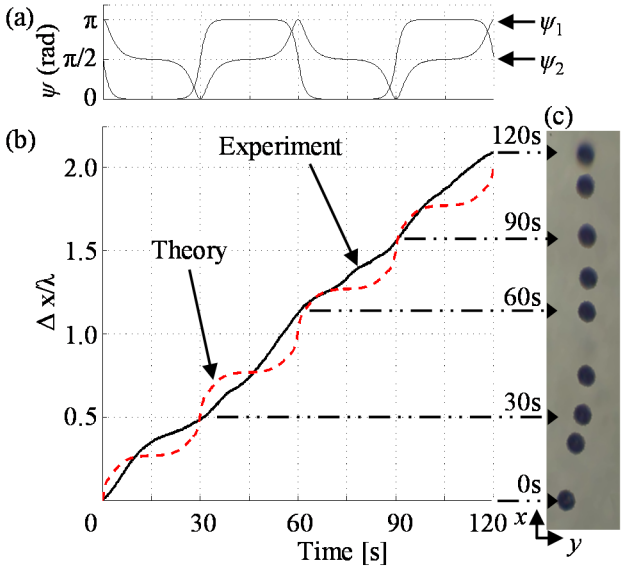

Figure 3.5: Experimental manipulation of a spherical particle in one dimension. Comparison of experimental and theoretical results. (a) The sequence of ultrasound transducer phases ψ_1 and ψ_2 as a function of time, and (b) the corresponding theoretical and experimental displacement of a particle trapped in a node of the standing ultrasound wave field. (c) A composite picture of snapshots in time of the particle as it traverses two wavelengths λ in the reservoir, demonstrating that the particle can be displaced multiple wavelengths by independently adjusting the phases of two opposing ultrasound transducers.

ultrasound wave field, as the node is displaced over two wavelengths by adjusting the phases as described in (a), and (c) shows a composite image made of snapshots in time of the particle as it traverses the two wavelength distance. This demonstrates experimentally that a particle can be manipulated over multiple wavelengths, when independently adjusting the ultrasound transducer phases. The experiment closely matches the theoretical trajectory of a particle trapped in the node of the ultrasound wave field, subject to the imposed sequence of ψ_1 and ψ_2. The slight difference between the theoretical and experimental particle displacement is likely the result of minute misalignment of the opposing ultrasound transducers, which may alter the standing ultrasound wave field pattern due to reflections of the waves from the reservoir walls. Furthermore, inertia and viscous drag, not included in the model, prevent the particle from instantaneously tracking

the displacement of the node of the ultrasound wave field, upon changing the ultrasound transducer phases. This results in a more continuous displacement of the particle than theoretically predicted.

Figure 3.6(a)-(d) shows the displacements $\Delta x/\lambda$ resulting from the four example trajectories (i)-(iv) identified in Fig. 3.3, and displays the ultrasound transducer phase sequences (left column) along with the corresponding displacements (solid line) and ultrasound wave field amplitudes (dashed lines) of the ultrasound wave field (right column). In Fig. 3.6 (a), the linear change in $\Delta\psi$ is enabled by adjusting ψ_2 and maintaining ψ_1 constant. The node is displaced up to $\Delta x/\lambda = 1/4$, but further adjustment of ψ_2 results in

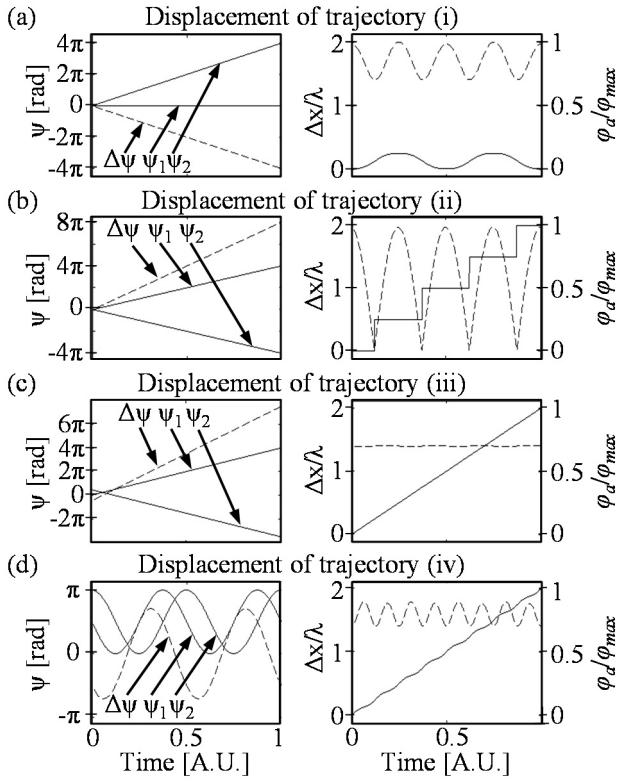

Figure 3.6: Particle displacements for different ultrasound transducer phase sequences. Sequence of ψ_1, ψ_2 and $\Delta\psi = \psi_1 - \psi_2$ for trajectories (i) - (iv) (Fig. 3.3) in the left column, with the corresponding displacement of a particle trapped in a node (solid line), and the amplitude of the ultrasound wave field (dashed line) in the right column. The ultrasound wave field amplitude has been normalized with the maximum ultrasound wave field

no additional displacement. In Fig. 3.6 (b) the linear change in $\Delta\psi$ is obtained by increasing ψ_1 and decreasing ψ_2 equally by $\Delta\psi$ /2. While a displacement of multiple wavelengths appears to be obtained, the phase combinations where the step-wise displacements occur correspond to a ultrasound wave field with zero amplitude, making controlled particle manipulation impossible. In Fig. 3.6 (c) each phase is adjusted similarly to Fig. 3.6 (b), with ψ_2 offset by an additional $\pi/2$, resulting in $\Delta\psi(0) \neq 0$. The nodal displacement is linear with respect to time, but the ultrasound wave field amplitude, while almost constant, never reaches the maximum possible value. Finally, in Fig. 3.6 (d), each phase is controlled independently along the trajectory shown in the inset of Fig. 3.3 (a), and experimentally demonstrated in Fig. 3.5. This sequence of phases results in nodal displacements over multiple wavelengths, and the ultrasound wave field amplitude is greater than or equal to that in the previous example. Note that the time scale of Fig. 3.5 (a) seems different from that of Fig. 3.6 (d). However, ψ_1 and ψ_2 follow the same sequence. Figure 3.6 shows that the values of ψ_1 and ψ_2 are more important than $\Delta\psi$, and that unconstrained manipulation of a particle trapped in a node cannot be achieved through linear adjustment of $\Delta\psi$, but can be realized through independent adjustment of ψ_1 and ψ_2. The ultrasound wave field amplitude of the standing wave depends on ψ_1 and ψ_2, and displacement of a particle cannot occur if the amplitude of the ultrasound wave field is zero. Although we performed this analysis for Eq. (3.7) the same methodology can be used for any $k \neq n\pi/L$ (Eq. (3.6)) to displace a particle over multiple wavelengths.

3.4 Conclusion

In conclusion, we have derived a theoretical model for the location of the nodes of a ultrasound wave field generated by two opposing ultrasound transducers with independent

control of the ultrasound transducer phases. A particle fixated at the node of the ultrasound wave field can be precisely displaced over multiple wavelengths, by adjusting the phases of the ultrasound transducers independently. As opposed to other methods in the literature, the theoretical model takes into account reflections normal to the ultrasound transducer surface, removing the need for complicated experimental implementations with, e.g., matching layers, backing layers, or offset ultrasound transducers. It is shown that when developing a sequence of ultrasound transducer phases to achieve a specific displacement trajectory, special consideration must be given to the ultrasound wave field amplitude of the standing wave. Using a simple experimental apparatus, it is demonstrated that a particle can be displaced over $\Delta x/\lambda = 2$, by applying a sequence of phase settings to both ultrasound transducers. Good agreement between the theoretically predicted and experimentally measured displacement is observed.

3.5 References

[3.1] L. P. Gor'kov, "On the Forces Acting on a Small Particle in an Acoustical Field in an Ideal Fluid," *Sov. Phys. Dokl*., vol. 6, pp. 773, 1962.

[3.2] K. Yoshika and Y. Kawashima, "Acoustic radiation pressure on a compressible sphere," *Acoustica*, vol. 5, pp. 167–173, 1955.

[3.3] F. Zheng, Y. Li, H.-S. Hsu, C. Liu, C. Tat Chiu, C. Lee, H. Ham Kim, and K. K. Shung, "Acoustic trapping with a high frequency linear phased array," *Appl. Phys. Lett*., vol. 101, pp. 214104, 2012.

[3.4] A. Grinenko, P. D. Wilcox, C. R. P. Courtney, and B. W. Drinkwater, "Proof of principle study of ultrasonic particle manipulation by a circular array device," *Proc. R. Soc. A.*, vol. 468, pp. 3571–3586, 2012.

[3.5] T. Kozuka, K. Yasui, T. Tuziuti, A. Towata, and Y. Iida, "Noncontact acoustic manipulation in air," *Jpn. J. Appl. Phys*., vol. 46, pp. 4948, 2007.

[3.6] C. R. P. Courtney, C.-K. Ong, B. W. Drinkwater, P. D. Wilcox, C. Demore, S. Cochran, P. Glynne-Jones, and M. Hill, "Manipulation of microparticles using phase-controllable ultrasonic standing waves," *J. Acoust. Soc. Am*., vol. 128, pp.

195-199, 2010.

[3.7] C. R. P. Courtney, C.-K. Ong, B. W. Drinkwater, A. L. Bernassau, P. D. Wilcox, and D. R. S. Cumming, "Manipulation of particles in two dimensions using phase controllable ultrasonic standing waves," *Proc. R. Soc. A*., vol. 468, pp. 337–360, 2012.

[3.8] A. Grinenko, C. K. Ong, C. R. P. Courtney, P. D. Wilcox, and B. W. Drinkwater, "Efficient counter-propagating wave acoustic micro-particle manipulation," *Appl. Phys. Lett.*, vol. 101, pp. 233501, 2012.

[3.9] L. E. Kinsler, A. R. Frey, A. B. Coppens, and J. V. Sanders, *Fundamentals of Acoustics*, NJ, USA: John Wiley, 2000.

[3.10] J. E. Mark, in *Polymer Data Handbook*, Oxford, UK: Oxford University Press, 2009, p. 1036.

CHAPTER 4

ULTRASOUND DIRECTED SELF-ASSEMBLY IN TWO DIMENSIONS

Adapted with permission from J. Greenhall, F. Guevara Vasquez, and B. Raeymaekers, "Ultrasound directed self-assembly of user-specified patterns of nanoparticles dispersed in a fluid medium," Appl. Phys. Lett. **108** 103103 (2016).

4.1 Introduction

To achieve the second objective of this dissertation, we introduce ultrasound directed self-assembly (DSA) for organizing user-specified patterns of nano- or microparticles in two dimensions (2D). This requires relating the arrangement and parameters (amplitude and phase) of the ultrasound transducers that generate the ultrasound wave field to the resulting pattern of particles that is assembled. This translates into two problems: (1) the "forward ultrasound DSA problem" entails calculating the pattern of particles resulting from user-specified ultrasound transducer parameters, and (2) the "inverse ultrasound DSA problem" involves calculating the ultrasound transducer parameters required to assemble a user-specified pattern of particles.

Solving the forward ultrasound DSA problem requires computing the acoustic radiation force associated with the ultrasound wave field generated by the ultrasound transducers. The resulting pattern of particles is then found as the stable fixed positions $\mathbf{x}_s$ of the acoustic radiation force, i.e., the location(s) where the force is zero and points toward $\mathbf{x}_s$ in the surrounding region [4.1]. The inverse ultrasound DSA problem is solved either directly or indirectly. Indirect methods solve the forward ultrasound DSA problem for a range of ultrasound transducer parameters to create a "map" that relates patterns of particles to those parameters [4.2]–[4.4]. Direct methods have only been derived for a small number of specific reservoir and/or pattern geometries [4.5]–[4.7], without providing a universal solution to the inverse ultrasound DSA problem. Thus, the objective of this chapter is to demonstrate a direct solution methodology to the inverse ultrasound DSA problem for a user-specified pattern in a two-dimensional, arbitrary, simple closed reservoir geometry and ultrasound transducer arrangement.

We relate the user-specified patterns of particles to the ultrasound transducer parameters in two steps. First we calculate the ultrasound wave field in an arbitrary shaped reservoir lined with ultrasound transducers around its perimeter as a function of the ultrasound transducer parameters using the boundary element method based on Green's third identity [4.8], which relates the wave field within a simple closed domain to the boundary conditions imposed on the perimeter of that domain. Then, we calculate the acoustic radiation force acting on a spherical particle to determine the pattern of particles resulting from the ultrasound wave field [4.1]. Finally, we compute the ultrasound transducer parameters required to assemble a user-specified pattern of particles by solving a constrained nonconvex quadratic optimization problem using eigendecomposition. We present a theoretical derivation and experimental validation. We clarify that the method presented in this chapter is unrelated to ambisonics [4.9], [4.10] and acoustic holography [4.11], where a user-specified acoustic wave field, rather than the stable fixed points of the acoustic radiation force, is related to the parameters of acoustic sources through unconstrained linear least squares optimization.

4.2 Forward ultrasound directed self-assembly problem

Figure 4.1 shows a two-dimensional arbitrary shaped reservoir filled with a fluid medium of density ρ_f and sound speed c_f, and with N_t ultrasound transducers of acoustic impedance Z_t around the perimeter. The inset of Fig. 4.1 illustrates the discretization of the domain perimeter S into $N_t \geq N_b$ boundary elements (black dots) and the domain D into N_d domain points (red dots), which may be selected in any arrangement. The j^{th} boundary element, identified by its center point $\mathbf{q}_j$, is $\varepsilon(\mathbf{q}_j)$ wide and is driven by the ultrasound

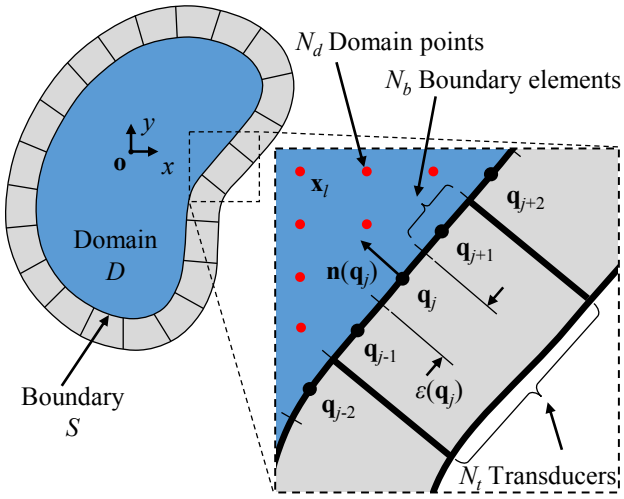

Figure 4.1: Schematic of the two-dimensional fluid reservoir. The reservoir has arbitrary geometry lined with N_t ultrasound transducers. The inset illustrates the discretization scheme of the boundary element method used to model the ultrasound directed self-assembly process, which divides the domain boundary into N_b boundary elements (black dots) and the domain into N_b domain points (red dots). Additionally, the inset shows the width $\varepsilon(\mathbf{q}_j)$ and normal direction $\mathbf{n}(\mathbf{q}_j)$ of the j^{th} boundary element $\mathbf{q}_j$.

transducer parameter $v(\mathbf{q}_j)$, i.e., the complex harmonic velocity (amplitude and phase) of the ultrasound transducer surface along its normal direction $\mathbf{n}(\mathbf{q}_j)$, which acts as a piston source to create the ultrasound wave field. Additionally, we indicate a test point $\mathbf{x}_l$ in D with respect to the reservoir origin $\mathbf{o}$.

We use the boundary element method to calculate the ultrasound wave field with frequency ω in terms of the time-independent, complex scalar velocity potential φ, at each domain point within D. We note that: (1) φ must satisfy the Helmholtz equation $(\nabla^2\varphi + k^2\varphi = 0)$ in D, where $k = \omega/c_f$ is the wave number of the ultrasound wave field in the fluid medium. (2) The impedance boundary condition $\partial\varphi/\partial\mathbf{n} + ik\tilde{Z}\varphi = v$ must be satisfied on S, where $\tilde{Z} = \rho_f c_f / Z_t$ is the impedance ratio, accounting for the absorption and reflection of the ultrasound wave within the fluid medium as it interacts with the ultrasound transducer surface. Arranging all ultrasound transducer parameters v into an $N_d \times 1$ array $\mathbf{v}$,

we calculate the ultrasound wave field at all N_d domain points as [4.8]

$$\boldsymbol{\varphi} = \mathbf{PWv}. \tag{4.1}$$

The matrix **W** maps each boundary element to its corresponding ultrasound transducer, i.e., $w_{jm} = 1$ if the j^{th} boundary element is contained within the m^{th} ultrasound transducer, otherwise $w_{jm} = 0$. Additionally, each term p_{ij} of the matrix **P** corresponds to the ultrasound wave field created at $\mathbf{x}_l$ by a point source located at $\mathbf{q}_j$ on S, including all reflections from the reservoir walls. We calculate all p_{lj} terms in matrix form as

$$\mathbf{P} = \hat{\mathbf{B}} - \hat{\mathbf{A}}\left(\tfrac{1}{2}\mathbf{I} + \mathbf{A}\right)^{-1}\mathbf{B}. \tag{4.2}$$

I is the identity matrix and we compute each term a_{lj} and b_{lj} of the matrices **A** and **B** as

$$a_{lj} = \left[ik\bar{Z}G\left(\mathbf{q}_j, \mathbf{x}_l\right) + \frac{\partial G\left(\mathbf{q}_j, \mathbf{x}_l\right)}{\partial \mathbf{n}(\mathbf{q}_j)} \right] \times \varepsilon\left(\mathbf{q}_j\right)\delta\left(\mathbf{q}_j, \mathbf{x}_l\right), \text{ and} \tag{4.3}$$

$$b_{ij} = G\left(\mathbf{q}_j, \mathbf{x}_l\right)\varepsilon\left(\mathbf{q}_j\right)\delta\left(\mathbf{q}_j, \mathbf{x}_l\right). \tag{4.4}$$

Here, $i = \sqrt{-1}$, $\delta(\mathbf{q}_j, \mathbf{x}_l) = 0$ when $\mathbf{q}_j = \mathbf{x}_l$, otherwise it is 1, and $G(\mathbf{q}_j, \mathbf{x}_l)$ is the Green's function, which represents the free-field ultrasound wave emitted from a point source located at $\mathbf{q}_j$ and measured at location $\mathbf{x}_l$, defined as [4.8]

$$G\left(\mathbf{q}_j, \mathbf{x}_l\right) = -\frac{i}{4}H_0\left(k\left|\mathbf{q}_j - \mathbf{x}_l\right|\right). \tag{4.5}$$

H_0 is the 0^{th} order Hankel function of the first kind, and $|\mathbf{q}_j - \mathbf{x}_l|$ is the distance between

points $\mathbf{q}_j$ and $\mathbf{x}_l$. We obtain the matrices $\hat{\mathbf{A}}$ and $\hat{\mathbf{B}}$ in Eq. (4.2) analogously to **A** and **B**, differing only by the selection of the points $\mathbf{x}_l$, which lie on S for **A** and **B**, and lay in D for $\hat{\mathbf{A}}$ and $\hat{\mathbf{B}}$. Thus, using the boundary element method we relate the ultrasound transducer parameters to the resulting ultrasound wave field.

To relate the ultrasound wave field to the pattern of particles, we calculate the acoustic radiation force acting on a particle of radius r_p, density ρ_p, and sound speed c_p, dispersed in a fluid medium at location $\mathbf{x}_l$ in D using Eq. (1.3), where the acoustic radiation potential U_l at $\mathbf{x}_l$ is written in vector form as

$$U_l = \mathbf{v}^H \mathbf{Q}_l \mathbf{v} . \tag{4.6}$$

Here, $\mathbf{v}^H$ is the conjugate transpose of **v**, and the Hermitian matrix $\mathbf{Q}_l$ is calculated as

$$\begin{aligned} \mathbf{Q}_l = 2\pi r_p^3 \rho_f \mathbf{W}^H \Bigg\{ & \frac{1}{3} k^2 \left[1 - \left(\frac{\beta_p}{\beta_f} \right)^2 \right] \left[\mathbf{p}_l \mathbf{p}_l^H \right] \\ & - \left[\frac{\rho_p - \rho_f}{2\rho_p + \rho_f} \right] \left[\left(\frac{\partial \mathbf{p}_l}{\partial x} \right) \left(\frac{\partial \mathbf{p}_l}{\partial x} \right)^H + \left(\frac{\partial \mathbf{p}_l}{\partial y} \right) \left(\frac{\partial \mathbf{p}_l}{\partial y} \right)^H \right] \Bigg\} \mathbf{W} \end{aligned} . \tag{4.7}$$

$\mathbf{p}_l^H$ is the l^{th} row of $\mathbf{P}$, and $\beta_f = 1/\rho_f c_f$ and $\beta_p = 1/\rho_p c_p$ are the compressibility of the fluid medium and particle, respectively. From Eq. (4.6), we calculate the obtained pattern of particles as the region(s) consisting of points $\mathbf{x}_l$, where U_l is locally minimum.

4.3 Inverse ultrasound directed self-assembly problem

To achieve assembly of a user-specified pattern of particles consisting of the set of desired positions X_{des}, each value U_l corresponding to each position $\mathbf{x}_l \in X_{des}$, must be

locally minimum. We relax the requirement of local minimality to obtain an optimization problem with a single objective function by minimizing the average value of U_l for all points $\mathbf{x}_l \in X_{des}$, which is written as the quadratic function

$$\bar{U} = \mathbf{v}^H \bar{\mathbf{Q}} \mathbf{v}, \tag{4.8}$$

where the matrix $\bar{\mathbf{Q}}$ is the average of the matrices $\mathbf{Q}_l$ corresponding to each desired position $\mathbf{x}_l \in X_{des}$. $\bar{U}$ has no lower bound because $\bar{\mathbf{Q}}$ is indefinite. Physically, this means that particles assemble at the desired positions more effectively by increasing the harmonic velocity amplitude of the ultrasound transducer surfaces indefinitely ($|\mathbf{v}| \to \infty$). Practically, the function generator that energizes the ultrasound transducers limits the harmonic velocity amplitude of the ultrasound transducer surfaces to finite values. Thus, we constrain the magnitude $|\mathbf{v}| = \alpha$, where α is a real, scalar value representing the maximum harmonic velocity of the ultrasound transducer surface that can be achieved with a function generator. Hence, we formulate the constrained quadratic optimization problem

$$\min \bar{U}, \text{ subject to } |\mathbf{v}| = \alpha. \tag{4.9}$$

From Eq. (4.9), we calculate the ultrasound transducer parameters **v*** required to assemble a user-specified pattern of particles as the eigenvector corresponding to the smallest eigenvalue of $\bar{\mathbf{Q}}$, where **v*** has length α [4.12]. Because **v*** minimizes U_l averaged over the desired positions $\mathbf{x}_l \in X_{des}$, it will result in the largest possible acoustic radiation force driving the particles to the desired positions, for a given ultrasound transducer magnitude $|\mathbf{v}| = \alpha$.

4.4 Simulated two-dimensional patterns of particles

We implement the forward and inverse ultrasound DSA techniques by developing a scientific tool with user-friendly graphical user interface (GUI). The GUI enables a user to specify the material properties, and the frequency and arrangement of ultrasound transducers that line a square reservoir. Within the reservoir, the user specifies a pattern of particles, and the GUI solves the inverse ultrasound DSA problem (Eq. 4.9) to calculate the ultrasound transducer parameters necessary to achieve the user-specified pattern. Additional details regarding the GUI can be found in Section 4.8.

To demonstrate assembly of a complex user-specified pattern of particles, we define the University of Utah "U" logo within a square water-filled reservoir with $N_t = 200$ ultrasound transducers around the perimeter, and compute the ultrasound transducer parameters **v*** required to assemble this pattern using Eq. (4.9). Figure 4.2 shows the simulated pattern of particles resulting from the computed ultrasound transducer parameters **v*** (black) and the corresponding acoustic radiation potential (green), together with the user-specified "U" pattern (red). We qualitatively observe a close match between

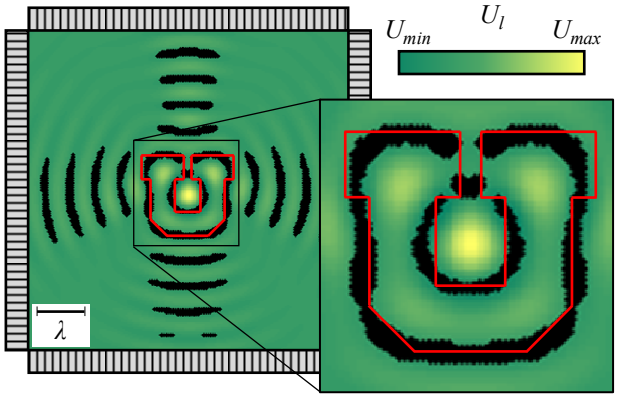

Figure 4.2: Simulated two-dimensional user-specified pattern of particles. Ultrasound directed self-assembly (DSA) of a University of Utah "U" pattern of particles. We compute the ultrasound transducer parameters **v*** required to assemble a user-specified "U" pattern (red) using the inverse ultrasound DSA method, and then simulate the acoustic radiation potential (green) generated by those parameters, which drives particles into the simulated

the user-specified and simulated patterns, except at sharp edges of the pattern. When $\rho_p \neq \rho_f$ and $\beta_p \neq \beta_f$, the ultrasound DSA technique is limited to creating pattern features with finite curvature, and the minimum achievable pattern radius is inversely proportional to the frequency of the ultrasound wave. This limitation is easily shown in the case of a concentric-circular pattern of particles, which is achieved by generating a standing ultrasound wave consisting of a 0^{th} order Bessel function of the first kind. In this standing wave, particles are organized into a pattern of concentric circles whose radii correspond to the zeros of the Bessel function. The maximum achievable curvature will coincide with the circle created at the first zero of the Bessel function, with radius $R = 2.4048 \cdot c_f/\omega$. Thus, we show that the minimum achievable pattern radius is inversely proportional to the frequency of the ultrasound wave. Extra features, not part of the user-specified pattern, may exist if the optimization (Eq. (4.9)) does not yield an exact match with the user-specified pattern for the specified ultrasound transducer arrangement, operating frequency ω, and reservoir geometry.

4.5 Experimental two-dimensional patterns of particles

Figure 4.2 illustrates that the method enables creating complex patterns of particles However, the ability to create a complex pattern of particles increases asymptotically with an increasing number of ultrasound transducers, and a large number of ultrasound transducers is often required. Thus, to validate our model and method, we limit the experiments to $N_t = 4$ and 8 and focus on dot and line patterns of particles, which are commonly prescribed patterns in engineering applications [4.13]–[4.18]. Figure 4.3 shows a schematic of the experimental procedure. We define a user-specified pattern in a square

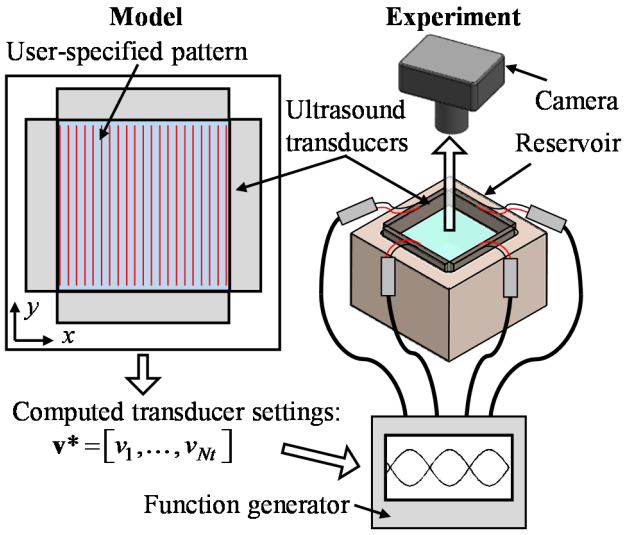

Figure 4.3: Schematic of the two-dimensional experimental apparatus. Experimental validation of the inverse ultrasound directed self-assembly (DSA) method is accomplished using a square reservoir filled with water and dispersed 80 nm carbon particles. A user-specified pattern is defined in the model and the ultrasound transducer parameters to obtain this pattern are computed using the inverse ultrasound DSA method (Eq. (4.10)). The ultrasound transducer parameters are then applied to the experimental setup, assembling a pattern of particles, which is then compared to the user-specified pattern.

reservoir filled with water and 80 nm carbon particles, lined with ultrasound transducers (PZT type SM112) with center frequency $\omega/2\pi$ = 1.5 MHz. The ultrasound transducer parameters $\mathbf{v}^* = \left[v_1, v_2, \ldots, v_{N_t}\right]^T$ obtained by solving Eq. (4.9) are applied to the N_t ultrasound transducers using a function generator, and we record the assembled pattern of particles using a camera, and compare it to the user-specified pattern.

Figure 4.4 shows two example patterns in a 12.75×12.75 mm square reservoir with N_t = 4. Feasible patterns for this ultrasound transducer arrangement include lines spaced $\lambda/2$ apart, parallel to a reservoir wall (Fig. 4.4(a)), and dots arranged in a square grid formation spaced $\lambda/2$ apart (Fig. 4.4(b)). Additionally, using a 24.75×24.75 mm square reservoir with N_t = 8 enables assembly of more complex patterns, such as a curved line pattern (Fig. 4.5(a)), and a mixed line/dot pattern (Fig. 4.5(b)). Figures 4.4 and 4.5 show the user-

specified pattern (red) and experimentally obtained pattern (black) assembled using the computed ultrasound transducer parameters. The insets show a magnified view of the user-specified pattern superimposed on the experimentally obtained patterns. Tables 4S.1 - 4S.6 in section 4.9 list the calculated ultrasound transducer parameters **v***, i.e., the amplitude and phase of the harmonic velocity of the ultrasound transducer surface, which correspond with the experiments shown in Figs. 4.4 and 4.5, respectively, and show that nontrivial ultrasound transducer parameters are required to assemble seemingly intuitive user-specified patterns of particles.

4.6 Ultrasound directed self-assembly pattern error

To quantify the accuracy of the experimentally obtained pattern of particles with respect to the user-specified pattern, we calculate the pattern error E_{pat} as the average distance between the centers of the user-specified and experimentally obtained pattern features (lines or dots), normalized by the nominal pattern spacing λ/2, for lines and dot patterns shifted in the *x*- and *y*-direction. Fig. 4.6 shows the pattern error as a function of the normalized pattern shift distance $\Delta x/\lambda \in [0, 1/2)$ for line (triangle marker) and dot (dot marker) patterns. Tables 4S.5-4S.6 in Section 4.9 list the calculated ultrasound transducer parameters **v***. The pattern error E_{pat} is less than 16.0% and 16.5% for line and dot patterns, respectively, indicating good agreement between the user-specified and experimentally assembled patterns of particles. The pattern error results from slight misalignment of the ultrasound transducers within the reservoir, and from the ultrasound transducers not performing as perfect piston sources, as assumed in the theoretical model. We also note that it is possible for the experimentally obtained pattern to contain additional pattern features, not part of the user-specified pattern. For instance, it is possible to assemble a

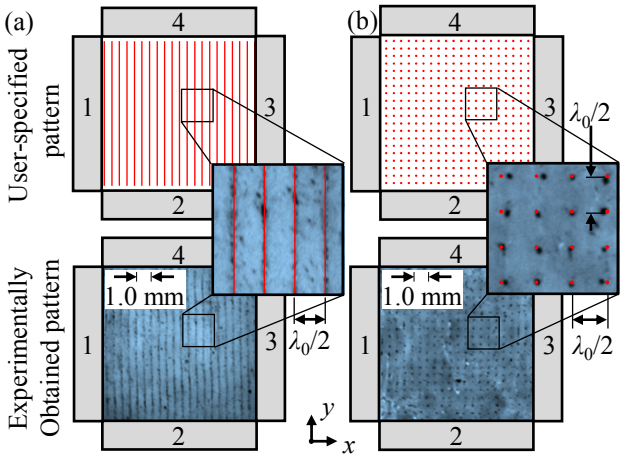

Figure 4.4: Experimentally obtained line and dot patterns. User-specified patterns (red) and corresponding experimentally obtained patterns (black) assembled with the ultrasound transducer parameters calculated with the inverse ultrasound directed self-assembly method for a (a) line pattern, (b) dot pattern of particles. Tables 4S.1 and 4S.2 in Section 4.9 list the ultrasound transducer parameters **v*** to assemble the pattern of particles.

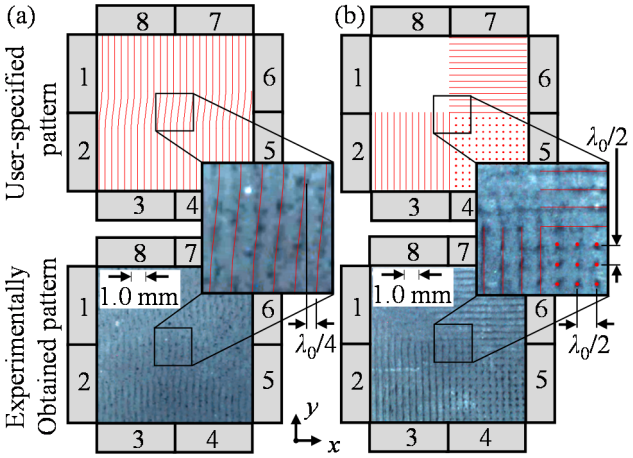

Figure 4.5: Experimentally obtained shifted-line and a dot/line combination patterns. User-specified patterns (red) and corresponding experimentally obtained patterns (black) assembled with the ultrasound transducer parameters calculated with the inverse ultrasound directed self-assembly method for a (a) shifted line pattern, (b) mixed line/dot pattern of particles. Tables 4S.3 and 4S.4 in Section 4.9 list the ultrasound transducer parameters **v*** to assemble the pattern of particles.

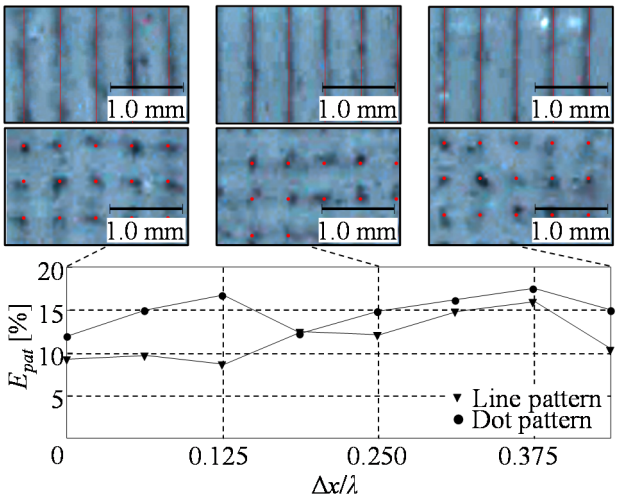

Figure 4.6: Experimentally obtained patterns shifted over user-specified distances. User-specified line and dot patterns (red) are shifted in increments of $\Delta x/\lambda = 0.0625$, and the ultrasound transducer parameters necessary to create those patterns are calculated using the inverse ultrasound directed self-assembly method and applied to the experimental setup, which results in the experimentally obtained patterns (black). We calculate the pattern error E_{pat} between the user-specified and experimentally obtained patterns is as a function of $\Delta x/\lambda$,and show images of the user-specified and experimentally obtained line and dot patterns for $\Delta x/\lambda = \{0.000, 0.250, 0.438\}$. Tables 4S.5 and 4S.6 list the ultrasound

user-specified dot pattern with spacing λ/2 by producing a line pattern that passes through the desired dot locations. In these instances, the pattern error is insufficient to account for the additional features, and a more complex scoring algorithm, such as a template matching method used in image processing, is desirable [4.19].

4.7 Conclusion

We have derived a method of directly solving the inverse ultrasound DSA problem that relates a user-specified pattern of nano- or microparticles in a fluid medium contained in an arbitrary shaped reservoir, to the operating parameters of any arrangement of ultrasound transducers. This method enables using ultrasound DSA to organize user-specified patterns of nano- or microparticles in a fluid medium, which accomplishes the second objective of this dissertation. This method contrasts with existing indirect methods that require

calculating complex maps of feasible patterns, and direct methods that only work for a limited set of reservoir and/or pattern geometries. In addition, the method accounts for all reflected waves, enabling experimental validation without requiring a complex setup with matching and backing layers to eliminate reflections. Thus, this method provides a practical approach of creating a user-specified pattern of particles using an arrangement of ultrasound transducers, in any reservoir geometry.

4.8 Supplemental software implementation of ultrasound directed self-assembly as a scientific tool

We implement the ultrasound directed self-assembly (DSA) in software as a scientific tool with a user-friendly graphical user interface (GUI). The scientific tool enables solving either the forward (Sec. 4.2), or the inverse ultrasound DSA problem (Sec. 4.3). Figure 4S.1 shows images of the GUI as it solves the forward (Fig. 4S.1(a)) and inverse ultrasound DSA problem (Fig. 4S.1(b)). In Fig. 4S.1(a), the user defines the parameters (amplitudes and phases) of the ultrasound transducers in the right-hand side of the GUI, and then the software tool solves the forward ultrasound DSA problem to calculate the resulting pattern of particles (cyan) and then display the pattern superimposed on the radiation potential (green) in the left-hand side of the GUI. In Fig. 4S.1(b), the user defines the user-specified pattern of particles by drawing dots or curves in the reservoir in the left-hand side of the GUI using a sketcher. The inverse ultrasound DSA problem is then solved to calculate the ultrasound transducer parameters necessary to achieve the user-specified pattern of particles. The GUI applies the computed parameters to the ultrasound transducers and solves the forward ultrasound DSA problem, to determine and display the actual pattern of particles (cyan) with the user-specified pattern of particles (red), superimposed over the

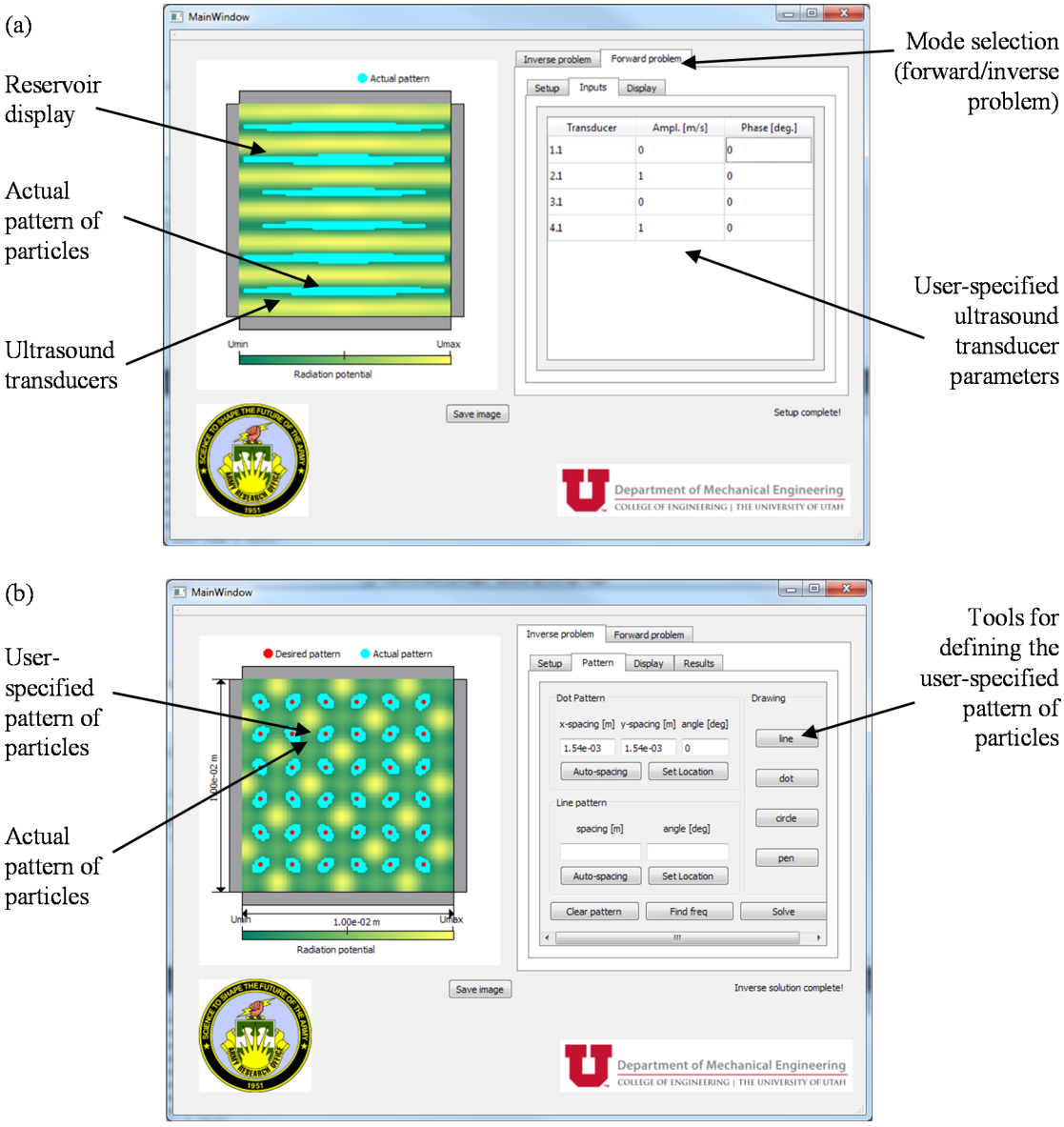

Figure 4S.1: Scientific tool and graphical user interface. Images of the scientific tool with a user-friendly graphical user interface (GUI) that enables solving (a) the forward ultrasound directed self-assembly (DSA) problem to determine the pattern of particles (cyan) that result from user-specified ultrasound transducer parameters, and (b) the inverse ultrasound DSA problem to calculate the ultrasound transducers necessary to achieve a user-specified pattern of particles (red).

ultrasound wave field (green) in the left-hand side of the GUI. The GUI facilitates adjustment of the material properties of the particles and fluid medium, and the arrangement and operating frequency of the ultrasound transducers lining the square reservoir.

4.9 Supplemental ultrasound transducer parameters

Table 4S.1: Ultrasound transducer parameters corresponding to Fig. 4.4(a)

T	Amplitude [m/s]	Phase [deg.]
1	0.70	-141.34
2	0.00	0.00
3	0.71	-142.96
4	0.00	0.00

Table 4S.2: Ultrasound transducer parameters corresponding to Fig. 4.4(b)

T	Amplitude [m/s]	Phase [deg.]
1	0.50	180.00
2	0.50	-2.29
3	0.50	177.70
4	0.50	0.00

Table 4S.3: Ultrasound transducer parameters corresponding to Fig. 4.5(a)

T	Amplitude [m/s]	Phase [deg.]
1	0.69	0.00
2	0.15	-15.36
3	0.00	0.00
4	0.00	0.00
5	0.69	0.00
6	0.15	-15.36
7	0.00	180.00
8	0.00	180.00

Table 4S.4: Ultrasound transducer parameters corresponding to Fig. 4.5(b)

T	Amplitude [m/s]	Phase [deg.]
1	0.00	180.00
2	0.49	32.29
3	0.00	0.00
4	0.51	32.29
5	0.51	32.29
6	0.00	-180.00
7	0.49	32.29
8	0.00	0.00

Table 4S.5: Ultrasound transducer parameters corresponding to the line patterns in Fig. 4.6

T / Δx	1		2		3		4	
	Amplitude [m/s]	Phase [deg.]	Amplitude [m/s]	Phase [deg.]	Amplitude [m/s]	Phase [deg.]	Amplitude [m/s]	Phase [deg.]
0	0.71	-146.69	0.00	1.52	0.71	-146.69	0.00	0.00
0.0625	0.71	-130.44	0.00	4.64	0.70	-125.05	0.00	0.00
0.125	0.75	-155.31	0.00	32.73	0.66	-125.08	0.00	0.00
0.1875	0.72	170.87	0.00	155.85	0.69	-19.99	0.00	0.00
0.25	0.71	15.30	0.00	-161.49	0.71	-164.69	0.00	0.00
0.3125	0.69	-19.99	0.00	155.85	0.72	170.87	0.00	0.00
0.375	0.66	-125.08	0.00	32.73	0.75	-155.31	0.00	0.00
0.4375	0.70	-125.05	0.00	4.64	0.71	-130.44	0.00	0.00

Table 4S.6: Ultrasound transducer parameters corresponding to the dot patterns in Fig. 4.6

T / Δx	1		2		3		4	
	Amplitude [m/s]	Phase [deg.]	Amplitude [m/s]	Phase [deg.]	Amplitude [m/s]	Phase [deg.]	Amplitude [m/s]	Phase [deg.]
0	0.50	0.00	0.50	-180.00	0.50	0.00	0.50	180.00
0.0625	0.51	0.00	0.49	-174.16	0.49	5.84	0.51	180.00
0.125	0.53	0.00	0.47	-149.99	0.47	30.00	0.53	180.00
0.1875	0.51	180.00	0.49	168.98	0.49	-11.02	0.51	0.00
0.25	0.57	-171.99	0.42	0.00	0.42	8.00	0.57	180.00
0.3125	0.49	0.00	0.51	11.02	0.51	-168.98	0.49	180.00
0.375	0.47	0.00	0.53	150.00	0.53	-30.00	0.47	180.00
0.4375	0.49	0.00	0.51	174.16	0.51	-5.84	0.49	180.00

4.10 References

[4.1] L. P. Gor'kov, "On the forces acting on a small particle in an acoustical field in an ideal fluid," Sov. Phys. Dokl. **6**, 773 (1962).

[4.2] J. Greenhall, F. Guevara Vasquez, and B. Raeymaekers, "Continuous and unconstrained manipulation of micro-particles using phase-control of bulk acoustic waves," Appl. Phys. Lett. **103**, 074103 (2013).

[4.3] T. Kozuka, K. Yasui, T. Tuziuti, A. Towata, and Y. Iida, "Noncontact acoustic manipulation in air," Jpn. J. Appl. Phys. Part 1 Regul. Pap. Short Notes Rev. Pap. **46**, 4948–4950 (2007).

[4.4] Grinenko, C. K. Ong, C. R. P. Courtney, P. D. Wilcox, and B. W. Drinkwater, "Efficient counter-propagating wave acoustic micro-particle manipulation," Appl. Phys. Lett. **101**, 233501 (2012).

[4.5] R. P. Courtney, B. W. Drinkwater, C. E. M. Demore, S. Cochran, A. Grinenko, and P. D. Wilcox, "Dexterous manipulation of microparticles using Bessel-function acoustic pressure fields," Appl. Phys. Lett. **102**, 123508 (2013).

[4.6] R. P. Courtney, C. E. M. Demore, H. Wu, A. Grinenko, P. D. Wilcox, S. Cochran, and B. W. Drinkwater, "Independent trapping and manipulation of microparticles using dexterous acoustic tweezers," Appl. Phys. Lett. **104**, 154103 (2014).

[4.7] Marzo, S. A. Seah, B. W. Drinkwater, D. R. Sahoo, B. Long, and S. Subramanian, "Holographic acoustic elements for manipulation of levitated objects," Nat. Commun. **6**, 8661 (2015).

[4.8] L. C. Wrobel, *The Boundary Element Method, Applications in Thermo Fluids and Acoustics*, NJ, USA: John Wiley & Sons, 2002.

[4.9] M. A. Gerzon, "Ambisonics in multichannel broadcasting and video," *J. Audio Eng. Soc.,* vol. 33, pp. 859, 1985.

[4.10] O. Kirkeby and P. A. Nelson, "Reproduction of plane wave sound fields," J. *Acoust. Soc. Am*., vol. 94, pp. 2992–3000, 1993.

[4.11] J. D. Maynard, E. G. Williams, and Y. Lee, "Nearfield acoustic holography: I. Theory of generalized holography and the development of NAH," *J. Acoust. Soc. Am*., vol. 78, pp. 1395–1413, 1985.

[4.12] N. Parlett, *The Symmetric Eigenvalue Problem*, NJ, USA: Prentice-Hall, Inc., 1998.

[4.13] M. Evander and J. Nilsson, "Acoustofluidics 20: Applications in acoustic trapping," *Lab. Chip*, vol. 12, pp. 4667, 2012.

[4.14] Y. Yamakoshi, Y. Koitabashi, N. Nakajima, and T. Miwa, "Yeast cell trapping in

ultrasonic wave field using ultrasonic contrast agent," *Jpn. J. Appl. Phys*., vol. 45, pp. 4712, 2006.

[4.15] Y. Yamakoshi, N. Nakajima, and T. Miwa, "Microbubble trapping by nonlinear bubble oscillation using pumping wave," *Jpn. J. Appl. Phys*., vol. 46, pp. 4847, 2007.

[4.16] V. M. Shalaev, "Optical negative-index metamaterials," *Nat. Photonics*, vol. 1, pp. 41–48, 2007.

[4.17] S. J. Corbitt, M. Francoeur, and B. Raeymaekers, "Implementation of optical dielectric metamaterials: A review," *J. Quant. Spectrosc. Radiat. Transf*., vol. 158, pp. 3–16, 2015.

[4.18] M. D. Haslam and B. Raeymaekers, "Aligning carbon nanotubes using bulk acoustic waves to reinforce polymer composites," *Compos. Part B Eng*., vol. 60, pp. 91–97, 2014.

[4.19] R. Brunelli, *Wiley: Template Matching Techniques in Computer Vision: Theory and Practice*, NJ, USA: John Wiley & Sons, Ltd., 2009.

CHAPTER 5

3D PRINTING MACROSCALE ENGINEERED MATERIALS USING ULTRASOUND DIRECTED SELF-ASSEMBLY AND STEREOLITHOGRAPHY

Adapted from J. Greenhall and B. Raeymaekers, "3D printing macroscale engineered materials using ultrasound directed self-assembly and stereolithography," Adv. Mater. Technol. **2** 1700122 (2017).

5.1.Introduction

In this chapter we address the third objective of the dissertation by integrating ultrasound directed self-assembly (DSA) with stereolithography (SLA) to enable 3D printing polymer matrix engineered materials with complex 3D geometry and user-specified microstructure.

Manufacturing engineered materials consisting of patterns of nano- or microparticles embedded in a matrix material (see Sec. 1.1) has been achieved via three different categories of techniques. Subtractive techniques such as focused-ion beam milling enable fabricating features with ultrafine resolution (<100 nm). Since each feature must be individually created, the technique requires long fabrication times and, thus, limits dimensional scalability of the material specimens [5.1], [5.2]. Additive techniques such as interference lithography and nanoimprint lithography enable rapid patterning of features over large ($\leq$ 1 cm^2) areas, but only work for a limited selection of materials and are typically restricted to organizing 2D patterns of features, thus constraining the material properties that can be tailored [5.2]–[5.4]. Alternatively, DSA techniques including templated DSA, template-free DSA, and external field DSA techniques based on electric and magnetic fields have been used to organize user-specified patterns of nano- or microparticles (see Sec. 1.4.1 for details) [5.5]. However, templated DSA is not dimensionally scalable due to template sizes on the order of nanometers or micrometers. Template-free DSA techniques only work with a limited selection of patterns of particles, which limits the material properties that can be tailored. Electric and magnetic field DSA techniques require ultrahigh amplitude fields and require conductive and ferromagnetic particles, thus, limiting the scalability and particle material choice. As such, existing

manufacturing techniques are constrained by material choice, the patterns of particles or features that can be fabricated, long fabrication times, dimensional scalability, and/or limited control of the macroscale geometry of the material specimen.

In contrast, ultrasound DSA employs the acoustic radiation force associated with an ultrasound wave field to assemble patterns of particles independent of the particle material properties [5.6]. Also, ultrasound DSA is scalable because it does not require a high amplitude ultrasound wave field to organize patterns of particles in low-viscosity (bulk and shear) fluids [5.7]. Combining ultrasound DSA with photo-curing enables organizing patterns of particles within a thin layer of liquid photopolymer resin, which is subsequently photo-cured to polymerize the resin and fixate the pattern of particles in place. Only simple 2D materials have been demonstrated using ultrasound DSA with photo-curing based on a laser that traces the desired specimen geometry, which limits implementing the materials in engineering applications that require 3D material structures [5.8], [5.9].

Thus, the objective of this chapter is to demonstrate a manufacturing process to 3D print macroscale engineered materials with complex 3D geometry and a tailored microstructure based on a user-specified pattern of particles embedded in a polymer matrix material. We integrate ultrasound DSA with SLA to 3D print materials in a layer-by-layer fashion. In each layer a user-specified 2D pattern enables tailoring the microstructure of the engineered material, unrestricted by material choice.

5.2.Ultrasound directed self-assembly/stereolithography manufacturing process

Figure 5.1 shows a schematic of the ultrasound DSA/SLA manufacturing process. An octagonal reservoir with L = 30.0 mm is lined with eight ultrasound transducers (PZT 4,

Steminc inc.) around its perimeter, and contains nickel-coated carbon fibers (Conductive Composites Company, Heber, UT) of length 100 μm and diameter 10 μm, dispersed via tip sonication (Hielscher UP200Ht) in liquid resin (Maker Juice Sub. G+) (Fig. 5.1(a)). We use a signal generator (Tektronix AFG3102) and radio-frequency amplifier (ENI A150) to energize two opposing ultrasound transducers (marked yellow in Fig. 5.1(a)) with a 25 V_{RMS} sinusoidal voltage at 1.65 MHz to generate a standing ultrasound wave field within the liquid resin. The acoustic radiation force associated with the ultrasound wave field drives the nickel-coated carbon fibers to the nodes of the standing ultrasound wave field (see Sec. 1.4.2) [5.6], [5.10], which results in a pattern of parallel lines of aligned nickel-coated carbon fibers spaced a half wavelength ($\lambda/2$ = 0.45 mm) apart in the liquid resin. A Digital Light Processing projector (ViewSonic PDJ7822HDL) exposes the liquid resin to visible/ultraviolet (UV) light through the transparent reservoir floor, which causes the liquid resin to cross-link and cure into a layer of thickness h_0 that fixates the pattern of particles in place [5.11] (inset image in Fig. 5.1(a)). The build plate lowers to $h_f > h_0$ above the transparent reservoir floor, and additional visible/UV light exposure cures the resin layer with thickness h_f to adhere it to the build plate (Fig. 5.1(b)). The build plate lifts out of the reservoir (Fig. 5.1(c)), and liquid resin replenishes the gap between the cured layer and the reservoir floor. We repeat the process shown in Fig. 5.1(a)-(c) to 3D print the engineered material layer-by-layer, where each layer contains a user-specified pattern of particles to enable tailoring the microstructure of the material (Fig. 5.1(d)) (video of the manufacturing process is available upon request). Furthermore, the SLA process allows controlling the macroscale geometry of the material.

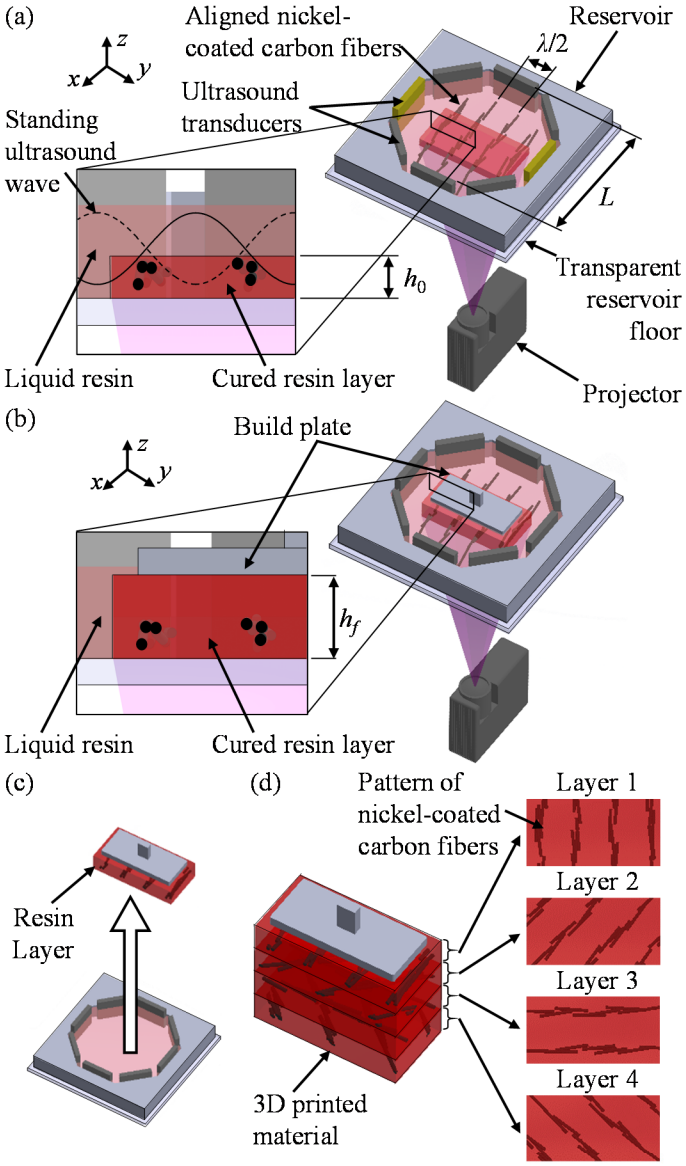

Figure 5.1: Ultrasound directed self-assembly/stereolithography manufacturing process. (a) The process sequentially employs ultrasound directed self-assembly to organize a user-specified pattern of aligned nickel-coated carbon fibers in a thin layer of resin contained in a reservoir, and (b) cures and (c) lifts the layer of resin to (d) fabricate materials layer-by-layer via stereolithography.

5.3.Single-layer engineered materials with user-specified microstructure

To demonstrate the capability of the ultrasound DSA/SLA manufacturing process for fabricating macroscale user-specified patterns within each material layer, we fabricate 8.00 × 5.00 × 0.45 mm single-layer material specimens containing line patterns of nickel-coated carbon fibers with 1.0 weight percent (wt. %), and 9.00 × 9.00 × 0.45 mm material specimens with complex user-specified patterns of nickel-coated carbon fibers containing with 1.0 wt. %. Figure 5.2(a) shows optical images of single-layer material specimens containing line patterns of aligned nickel-coated carbon fibers (length 100 μm, diameter 10 μm) with user-specified orientation angle $\theta_d = 0°$, 45°, 90°, and -45°, respectively. Inset images indicate the active pair of ultrasound transducers to organize each line pattern in yellow. We quantify the alignment of the nickel-coated carbon fibers in each material specimen shown in Fig. 5.2(a) using the 2D fast Fourier transform (FFT) to measure anisotropy in each of the optical images [5.12] (see Section 5.9 for details). Figure 5.2(b) shows the FFT anisotropy as a function of the angle θ, measured with reference to the vertical, for each of the material specimens shown in Fig. 5.2(a) with $\theta_d = 0°$ (red diamond marker), 45° (green square), 90° (yellow circle), and -45° (blue triangle). We quantify the angle at which the FFT is maximum and the full width at half maximum of the FFT anisotropy distribution for each single-layer material specimen. The difference between the angle at which the FFT is maximum and the user-specified angle is 1.62°, 0.59°, 1.89°, and 5.54° for $\theta_d = 0°$, 45°, 90°, and -45°, respectively, indicating excellent alignment of the line patterns of nickel-coated carbon fibers in the user-specified direction. The corresponding full width at half maximum, which indicates how well the individual nickel-coated carbon

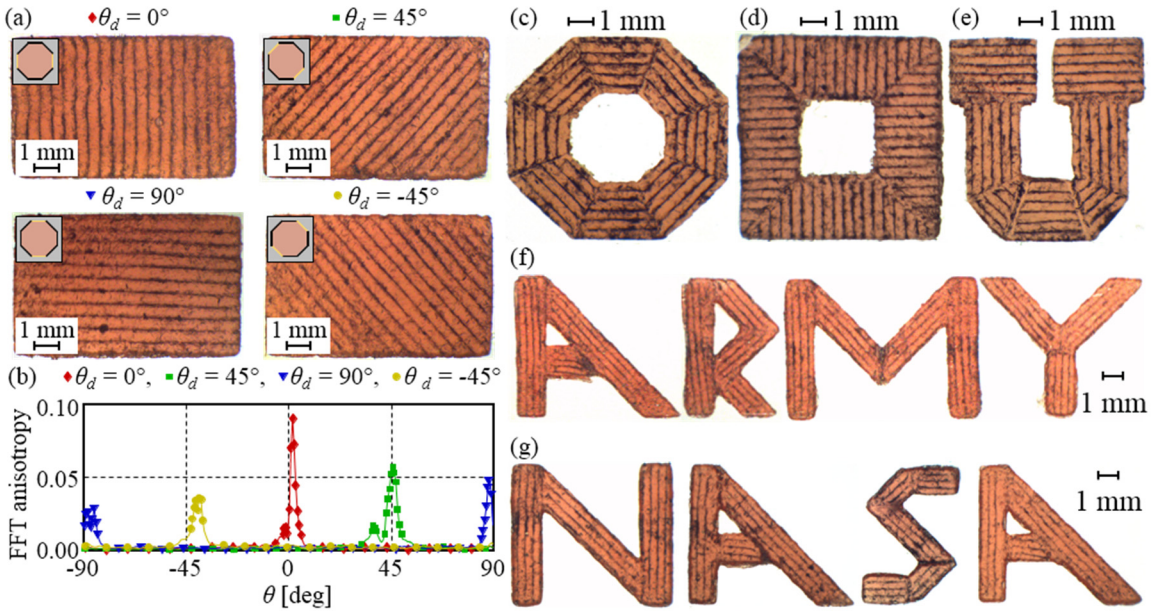

Figure 5.2: Single-layer material specimens with user-specified microstructure. (a) Material specimens containing line patterns of aligned nickel-coated carbon fibers oriented in user-specified angles θ_d = 0°, 45°, 90°, and -45°. (b) FFT anisotropy of each material specimen as a function of the image angle θ. Material specimens containing complex patterns of aligned nickel-coated carbon fibers organized into (c) octagonal, (d) triangular, (e) the University of Utah "U-logo" configurations, and the logos of (f) the Army and (g) NASA.

fibers are aligned with the angle at which the FFT is maximum, is 2.16°, 5.32°, 8.65°, and 5.05°, respectively, demonstrating good alignment. Figure 5.2(a) shows regions with locally non-straight lines and non-uniform nickel-coated carbon fiber concentrations. These defects are due to near-field effects [5.7], acoustic streaming [5.13], and squeeze flow of the liquid resin as the build plate is lowered into the reservoir (Fig. 5.1(b)), which may displace the nickel-coated carbon fibers and disrupt the resulting patterns within each resin layer.

In addition to simple line patterns, the ultrasound DSA/SLA manufacturing process enables organizing complex patterns of particles that cover macroscale areas. We accomplish this by fabricating the resin layer in multiple sections, where each section

contains a line pattern of particles with a user-specified orientation angle θ_d. Figure 5.2(c)-(g) shows optical images of single-layer material specimens with nickel-coated carbon fibers organized into complex patterns, including an octagon (Fig. 5.2(c)), triangle (Fig. 5.2(d)), the University of Utah "U-logo" (Fig. 5.2(e)), and the logos of the Army (Fig. 5.2(f)) and NASA (Fig. 5.2(g)), both of which have supported distinct aspects of the work we document in this dissertation.

In contrast with existing ultrasound DSA techniques based on phased arrays, which are limited to creating pattern features with nonsharp corners due to the ultrasound wave field interference patterns (see Sec. 4.4) [5.14], [5.15], the ultrasound DSA/SLA manufacturing process enables fabricating sharp features by combining multiple sections. However, Figs. 5.2(c)-(f) show small gaps (< 350 μm) between neighboring sections. These gaps prevent each section from colliding with neighboring sections as the build plate is lowered during the manufacturing process (Fig. 5.1(b)).

5.4.Multilayer engineered materials with user-specified microstructure

To demonstrate the capability of the ultrasound DSA/SLA manufacturing process for fabricating multilayer materials, we fabricate macroscale specimens containing Bouligand structures, which are found in biological structures and are known to provide, e.g., enhanced mechanical strength and puncture resistance [5.16]. Figure 5.3 shows four-layer specimens (8.0 × 5.0 × 1.8 mm) with a Bouligand microstructure consisting of line patterns of nickel-coated carbon fibers (1.0 wt. %) aligned in user-specified orientations θ_d = 0°, 90°,0°, and 90° (Fig. 5.3(a)), and θ_d = 0°, 45°, 90°, and -45° (Fig. 5.3(b)) in layers 1-4, respectively. Figure 5.3 shows trimetric views of the specimens imaged optically and via X-ray computed tomography (see Appendix D for details), and inset images show a top-

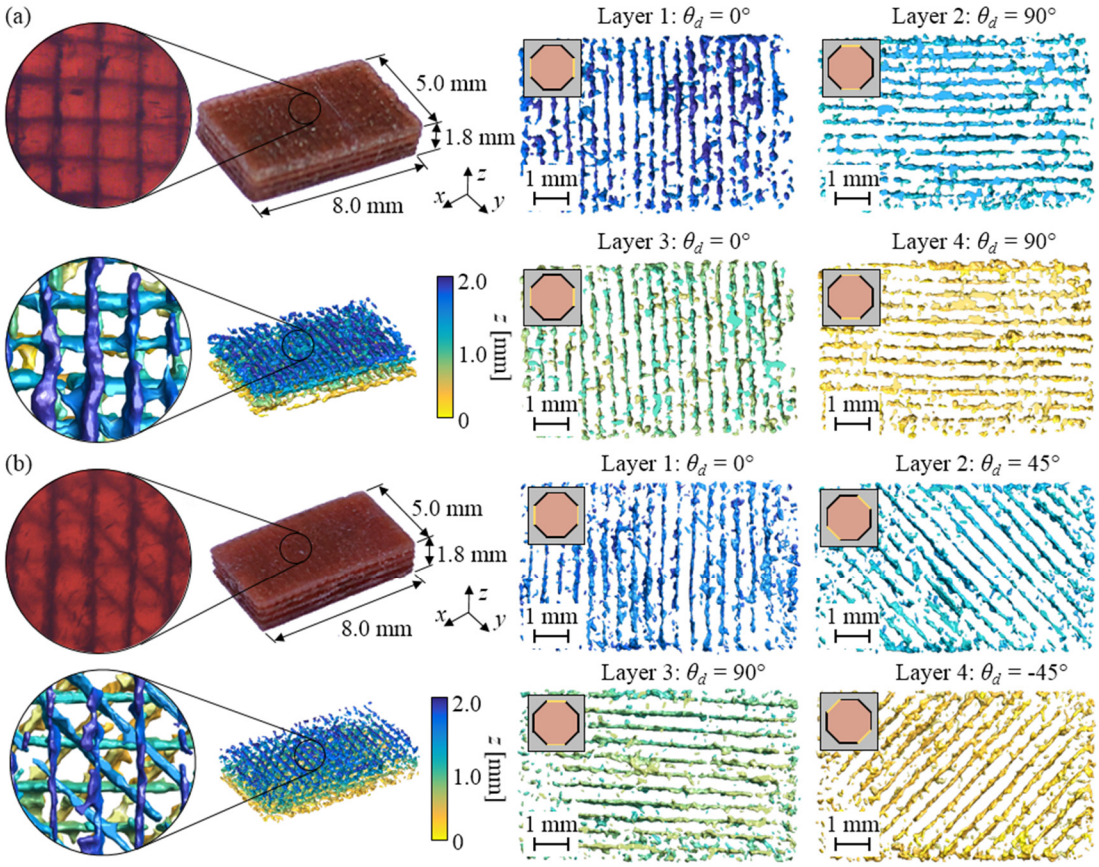

Figure 5.3: Multilayer engineered materials with user-specified microstructure. 3D printed multilayer material specimens containing Bouligand microstructures of aligned nickel-coated carbon fibers. (a) Four-layer material specimen containing line patterns with θ_d of 0°, 90°, 0°, and 90°, in layers 1-4, respectively. (b) Four-layer material specimen containing line patterns with user-specified alignment angles θ_d of 0°, 45°, 90°, and -45°, in layers 1-4, respectively.

view, where color represents the *z*-height in the specimen. Furthermore, Fig. 5.3 shows a top-view of each individual layer, with inset images indicating the pair of ultrasound transducers energized to create the line pattern, indicated in yellow. Imperfections in the line patterns occur for the same reasons discussed with single-layer material specimens (see Sec. 5.3). Additionally, limited resolution ($\geq 10 \times 10 \times 10$ μm voxel size) of the X-ray CT imaging may contribute to gaps between fibers or connected regions between lines in Fig. 5.3.

5.5.Engineered materials with tailored electrical conductivity

To demonstrate the possibilities of this manufacturing technique in the context of engineered materials with embedded functionality, we have fabricated a $5.00 \times 5.00 \times 0.35$ mm single-layer material specimen containing a line pattern of 2.0 wt. % aligned nickel-coated carbon fibers, which form a percolated network and enable tailoring the electrical conductivity of the material. We follow the manufacturing process shown in Fig. 5.1(a) to create a pattern of aligned nickel-coated carbon fibers via ultrasound DSA and then expose the liquid photopolymer resin to visible/UV light for 8 s to polymerize the resin and fixate the pattern of nickel-coated carbon fibers in place. We omit the final curing step shown in Fig. 5.1(b)-(d) to ensure that the line pattern of nickel-coated carbon fibers is not fully enclosed in resin, which would inhibit electrical resistance measurements. Figure 5.4 shows the electrical conductivity measurement process. We use a two-probe setup (Fig. 5.4(a)), where the probes are placed 1.0 mm apart along (1) a single line of nickel-coated carbon fibers to measure the "wire resistance" (Fig. 5.4(b)), and (2) on two neighboring lines of nickel-coated carbon fibers to measure the "insulator resistance" (Fig. 5.4(c)). We use a parameter analyzer (Kiethley 4200) to apply a voltage V_{app} sweep from -10 V to 10

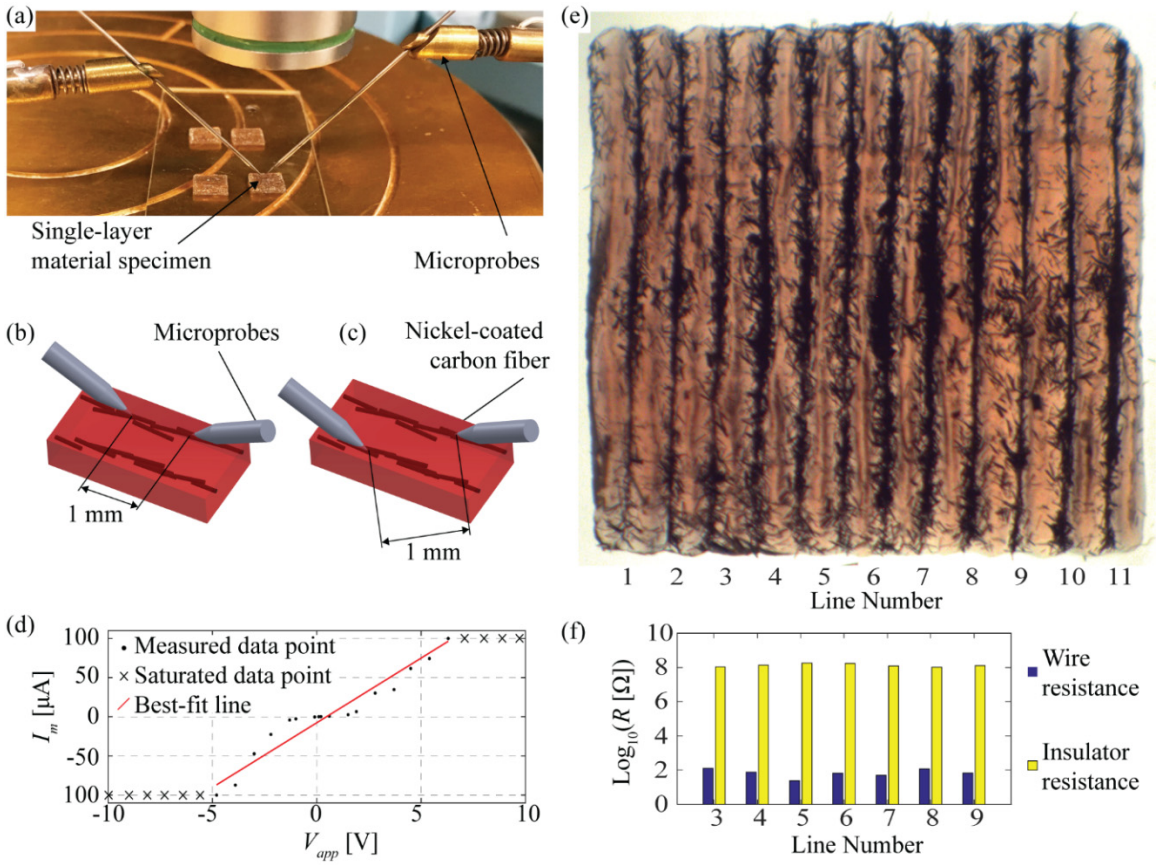

Figure 5.4: Engineered materials with tailored electrical conductivity. The process for measuring the electrical conductivity of engineered materials containing a line pattern of aligned nickel-coated carbon fibers uses (a) A two-probe setup with microprobes placed (b) along the same line of nickel-coated carbon fibers to measure the "wire resistance," or (c) along neighboring lines of nickel-coated carbon fibers to measure the "insulator resistance." (d) The resistance is measured using the slope of the line that best fits the applied voltage V_{app} and measured current I_m. (e) A single-layer material specimen containing a line pattern of aligned nickel-coated carbon fibers, with the line number indicated. (f) Measured wire (blue) and insulator resistances (yellow) for seven lines of aligned nickel-coated carbon fibers.

V, in 0.5 V increments, and measure the resulting electrical current I_m flowing between the probes. We calculate the resistance $R = V_{app}/I_m$ as the slope of the line that best fits the voltage-current data, which is calculated using ordinary least-squares linear regression (Fig. 5.4(d)) [5.17]. We limit the current amplitude to $|I_m| \leq 100$ mA to avoid damaging the parameter analyzer and, thus, we remove all data points for which the current measurement saturates at $I_m = \pm 100$ mA to avoid spurious resistance values. We repeat the electrical resistance measurements on a representative sample of seven lines of nickel-coated carbon fibers near the center of the material specimen to calculate the mean and standard deviation of the wire and insulator resistances (Fig. 5.4(e) and (f)). We measure an average wire resistance of 59.7 Ω and insulation resistance of 112.7 MΩ, with a standard deviation of 15.5 Ω and 23.2 MΩ, respectively, showing that the lines of aligned nickel-coated carbon fibers are conductive, yet insulated from each another. This example illustrates how the ultrasound DSA/SLA manufacturing process enables 3D printing materials with embedded insulated electrical wiring, or enables tailoring the conductivity of a material in specific directions.

5.6.Discussion of manufacturing process parameters

Scalability of the ultrasound DSA/SLA manufacturing process is achieved by enlarging the *z*-height of the ultrasound DSA/SLA apparatus and the reservoir size in the *x*- and *y*-directions. However, enlarging the reservoir incurs additional acoustic attenuation, which reduces the amplitude of the acoustic radiation force that assembles the patterns of particles [5.6], [5.7]. To mitigate the effects of acoustic attenuation we select a liquid photopolymer resin with low viscosity, and increase the input power applied to the ultrasound transducers. However, increased input power causes heat generation within the

ultrasound transducers, which can potentially damage the reservoir and/or cause boiling in the liquid photopolymer resin [5.18]. The ultrasound DSA/SLA manufacturing process time is primarily dependent on the curing and nickel-coated carbon fiber/liquid photopolymer resin dispensing rates. The curing times required for the initial (Fig. 5.1(a)) and final curing steps (Fig. 5.1(b)) depend on the photopolymer resin properties, the layer thickness h_f, and the weight fraction of carbon fibers, and are on the order of 7 s and 11 s, respectively, for the specimens shown in this chapter. In contrast to laser-based photo-curing processes, the curing time is independent of the x- and y- material dimensions [5.8], [5.9].

5.7.Conclusion

In conclusion, we have documented a manufacturing process based on integrating ultrasound DSA and SLA that, for the first time, enables 3D printing of engineered materials with arbitrary macroscale geometry and a user-specified microstructure based on a pattern of micro- or nanoparticles embedded in a polymer matrix material. We have illustrated the capability of the manufacturing process by 3D printing engineered materials containing a user-specified Bouligand microstructure and engineered materials with electrically-conductive lines of nickel-coated carbon fibers. In contrast with existing manufacturing techniques, the ultrasound DSA/SLA manufacturing process enables fabricating engineered materials with both macroscale complex 3D geometries and user-specified microstructure. Thus, the ultrasound DSA/SLA manufacturing process bridges the gap between engineered materials with unique physical properties demonstrated in a laboratory setting and macroscale engineering applications. This manufacturing process enables a broad range of applications including multifunctional composites, acoustic and

electromagnetic cloaking, and subwavelength imaging, among others.

5.8. Supplemental fast Fourier transform anisotropy quantification

Figure 5S.1 shows the process used to compute the fast Fourier transform (FFT) anisotropy for the material specimens shown in Fig. 5.2(a). We crop the images to the 4.5 × 4.5 mm region in the center of the image to remove edge effects (Fig. 5S.1(a)) and compute the 2D FFT of the image (Fig. 5S.1(b)). We perform a circular projection, wherein we sum the squared absolute values of the 2D FFT radially from the center of the 2D FFT in each direction to calculate the FFT anisotropy as a function of θ, and we normalize the FFT anisotropy so that the integral over $-\pi/2 \leq \theta \leq \pi/2$ has unit magnitude (Fig. 5S.1(c)).

5.9. Supplemental x-ray computed tomography details

To image the Bouligand structures shown in Fig. 5.3 we first use X-ray computed tomography (CT) (Varian BIR 150/130) to produce a 3D grayscale model of the material specimen, with lighter voxels representing nickel-coated carbon fibers and darker voxels representing resin. We threshold the 3D grayscale model to remove voxels with values

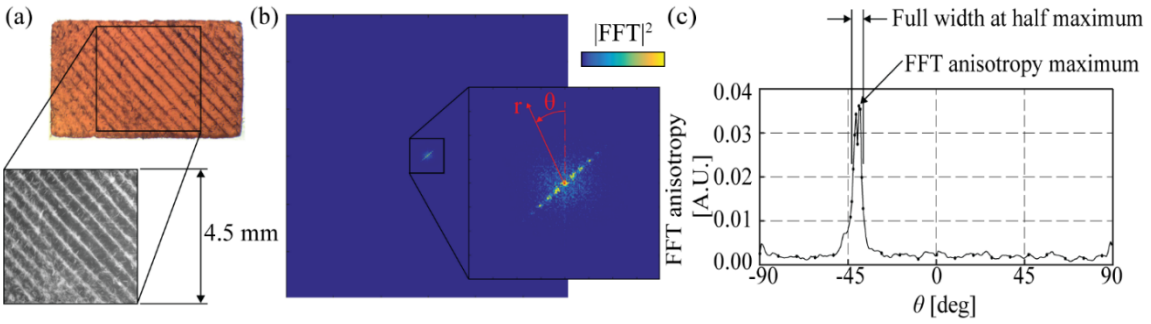

Figure 5S.1: Fast Fourier transform (FFT) anisotropy calculation. (a) A square section is cut from the original image and converted to gray scale. (b) The 2D FFT of the image is calculated. (c) The FFT anisotropy is calculated as a function of the image angle θ by summing $|FFT|^2$ radially from the center of (b), and the maximum and full width at half maximum are calculated.

below 30.0 % of the maximum voxel intensity in the 3D grayscale model to ensure that the width of the lines of nickel-coated carbon fibers in the X-ray CT images match those of the optical images. Finally, we generate isosurfaces around regions of connected voxels to create the X-ray CT images shown in Fig. 5.3.

5.10. References

[5.1] C. Enkrich, F. Pérez-Willard, D. Gerthsen, J. F. Zhou, T. Koschny, C. M. Soukoulis, M. Wegener, and S. Linden, "Focused-ion-beam nanofabrication of near-infrared magnetic metamaterials," *Adv. Mater*., vol. 17, pp. 2547–2549, 2005.

[5.2] Boltasseva and V. M. Shalaev, "Fabrication of optical negative-index metamaterials: Recent advances and outlook," *Metamaterials*, vol. 2, pp. 1–17, 2008.

[5.3] N. Feth, C. Enkrich, M. Wegener, and S. Linden, "Large-area magnetic metamaterials via compact interference lithography," *Opt. Express*, vol. 15, pp. 501–507, 2007.

[5.4] H. Schift, "Nanoimprint lithography: An old story in modern times? A review," *J. Vac. Sci. Technol. B Microelectron. Nanometer Struct*., vol. 26, pp. 458, 2008.

[5.5] M. Grzelczak, J. Vermant, E. M. Furst, and L. M. Liz-Marzán, "Directed self-assembly of nanoparticles," *ACS Nano*, vol. 4, pp. 3591–3605, 2010.

[5.6] L. P. Gor'kov, "On the forces acting on a small particle in an acoustical field in an ideal fluid," *Sov. Phys. Dokl*., vol. 6, pp. 773 1962.

[5.7] L. E. Kinsler, A. R. Frey, A. B. Coppens, and J. V. Sanders, *Fundamentals of Acoustics*, NJ, USA: John Wiley, 2000.

[5.8] M.-S. Scholz, B. W. Drinkwater, and R. S. Trask, "Ultrasonic assembly of anisotropic short fibre reinforced composites," *Ultrasonics*, vol. 54, pp. 1015–1019, 2014.

[5.9] T. M. Llewellyn-Jones, B. W. Drinkwater, and R. S. Trask, "3D printed components with ultrasonically arranged microscale structure," *Smart Mater. Struct*., vol. 25, pp. 02LT01, 2016.

[5.10] J. Greenhall, F. Guevara Vasquez, and B. Raeymaekers, "Dynamic behavior of microscale particles controlled by standing bulk acoustic waves," *Appl. Phys. Lett*., vol. 105, pp. 144105, 2014.

[5.11] J. V. Crivello and E. Reichmanis, "Photopolymer materials and processes for

advanced technologies," *Chem. Mater*., vol. 26, pp. 533–548, 2014.

[5.12] C. E. Ayres, B. Shekhar Jha, H. Meredith, J. R. Bowman, G. L. Bowlin, S. C. Henderson, and D. G. Simpson, "Measuring fiber alignment in electrospun scaffolds: a user's guide to the 2...," *J. Biomater. Sci. Polym. Ed*., vol. 19, pp. 603–621, 2008.

[5.13] L. Bernassau, P. Glynne-Jones, F. Gesellchen, M. Riehle, M. Hill, and D. R. S. Cumming, "Controlling acoustic streaming in an ultrasonic heptagonal tweezers with application to cell manipulation," *Ultrasonics*, vol. 54, pp. 268–274, 2014.

[5.14] J. Greenhall, F. Guevara Vasquez, and B. Raeymaekers, "Ultrasound directed self-assembly of user-specified patterns of nanoparticles dispersed in a fluid medium," *Appl. Phys. Lett*., vol. 108, pp. 103103, 2016.

[5.15] M. Prisbrey, J. Greenhall, F. Guevara Vasquez, and B. Raeymaekers, "Ultrasound directed self-assembly of three-dimensional user-specified patterns of particles in a fluid medium," *J. Appl. Phys*., vol. 121, pp. 014302, 2017.

[5.16] S. E. Naleway, M. M. Porter, J. McKittrick, and M. A. Meyers, "Structural design elements in biological materials: application to bioinspiration," *Adv. Mater*., vol. 27, pp. 5455–5476, 2015.

[5.17] W. Guo, C. Liu, X. Sun, Z. Yang, H. G. Kia, and H. Peng, "Aligned carbon nanotube/polymer composite fibers with improved mechanical strength and electrical conductivity," *J. Mater. Chem*., vol. 22, pp. 903–908, 2012.

[5.18] S.-W. Zhou and C. Rogers, "Heat generation, temperature, and thermal stress of structurally integrated piezo-actuators," *J. Intell. Mater. Syst. Struct*., vol. 6, pp. 372–379, 1995.

CHAPTER 6

CONCLUSION

In conclusion, this dissertation demonstrates a theoretical and experimental understanding of ultrasound directed self-assembly (DSA) to organize user-specified patterns of nano- or microparticles using the acoustic radiation force associated with an ultrasound wave field. The ability to manipulate nano- or microparticles and organize them into user-specified patterns has significant implications for biology, biomedical devices and process control, as well as fabricating engineered materials with unique physical properties that result from specific patterns of nano- and microparticles embedded in the material. The critical problem inhibiting manufacturing of these engineered materials is the ability to organize user-specified patterns of particles in a scalable manner to enable utilizing the engineered materials in macroscale engineering applications. In contrast with other DSA methods, ultrasound DSA is scalable due to the low ultrasound wave field amplitude required organize patterns of nano- or microparticles in a low-viscosity fluid, and ultrasound DSA works independent of the material properties of the nano- or microparticles.

We have theoretically derived the dynamic model of a spherical particle in a standing ultrasound wave field. Using this model, we observe that the acoustic radiation force drives the particle to the nodes or antinodes of the ultrasound wave field, where drag forces generated by the oscillating ultrasound wave field cause the particle to perpetually orbit the node or antinode. However, by operating at a moderate ultrasound wave field amplitude, we observe that the particle is essentially fixated at the node or antinode and, thus, we must control the location(s) of the nodes or antinodes to enable using ultrasound DSA to manipulate particles and organize them into user-specified patterns.

We have theoretically derived a method for using ultrasound DSA to manipulate

particles and organize them into user-specified patterns in 1D and 2D. In contrast with existing ultrasound DSA techniques, this method does not require reflected ultrasound waves to be removed from the reservoir, which greatly reduces the complexity of its practical implementation. Additionally, the 2D ultrasound DSA method enables organizing user-specified patterns of particles in a reservoir with arbitrary 2D geometry and ultrasound transducer arrangement, as opposed to existing ultrasound DSA techniques that only work for a specific pattern of particles, reservoir geometry and/or ultrasound transducer arrangement. However, we observe that the patterns of particles that can be achieved are constrained to patterns with nonsharp corners due to the interference patterns of the standing ultrasound wave fields, which have finite curvature. To mitigate this limitation, future work includes performing frequency optimization, employing ultrasound wave fields with multiple frequencies, and using a time-dependent sequence of ultrasound transducer parameters to organize complex user-specified patterns of particles.

Finally, we have integrated ultrasound DSA with stereolithography (SLA) as a manufacturing process to enable 3D printing macroscale engineered materials with unique physical properties. We demonstrate 3D printing multilayer engineered materials layer-by-layer, where each layer contains a user-specified pattern of particles. Additionally, we employ the ultrasound DSA/SLA manufacturing process to fabricate engineered material specimens containing parallel lines of aligned nickel-coated carbon fibers. We measure the "wire resistance" along each line of nickel-coated carbon fibers and the "insulator resistance" between neighboring lines of nickel-coated carbon fibers, and we observe low wire resistances (59.7 Ω average) and high insulator resistances (112.7 MΩ average). This demonstrates the feasibility of using the ultrasound DSA/SLA manufacturing process to

3D print macroscale structures with embedded electrical wiring. To improve the ultrasound DSA/SLA manufacturing process, future work includes interfacing the lines of nickel-coated carbon fibers with traditional electrical components, such as sensors, microcontrollers, and resistors, among others, to facilitate 3D printing structures with embedded electrical circuits.